

# Observations of the vertical distributions of summertime atmospheric pollutants in Nam Co: OH production and source analysis

Chengzhi Xing<sup>1</sup>, Cheng Liu<sup>1,2,3,4,\*</sup>, Chunxiang Ye<sup>5,\*</sup>, Jingkai Xue<sup>6</sup>, Hongyu Wu<sup>6</sup>, Xiangguang Ji<sup>7</sup>, Jinping Ou<sup>8</sup>, and Qihou Hu<sup>1</sup>

<sup>1</sup> Key Lab of Environmental Optics & Technology, Anhui Institute of Optics and Fine Mechanics, Hefei Institutes of Physical Science, Chinese Academy of Sciences, Hefei, 230031, China

<sup>2</sup> Department of Precision Machinery and Precision Instrumentation, University of Science and Technology of China, Hefei, 230026, China

<sup>3</sup> Center for Excellence in Regional Atmospheric Environment, Institute of Urban Environment, Chinese Academy of Sciences, Xiamen, 361021, China

<sup>4</sup> Key Laboratory of Precision Scientific Instrumentation of Anhui Higher Education Institutes, University of Science and Technology of China, Hefei, 230026, China

<sup>5</sup> College of Environmental Sciences and Engineering, Peking University, 100871 Beijing

<sup>6</sup> School of Environmental Science and Optoelectronic Technology, University of Science and Technology of China, Hefei, 230026, China

<sup>7</sup> Institute of Physical Science and Information Technology, Anhui University, Hefei, 230601, China

<sup>8</sup> The Department of Health Promotion and Behavioral Sciences, School of Public Health, Anhui Medical University, Hefei, 230032, China

\*Corresponding author. E-mail: chliu81@ustc.edu.cn; c.ye@pku.edu.cn

## 1 Abstract

2 The Tibetan Plateau (TP) plays a key role in regional environment and global climate change, however,  
3 the lack of vertical observation of atmospheric species, such as HONO and O<sub>3</sub>, hinders a deeper  
4 understanding of the atmospheric chemistry and atmospheric oxidation capacity (AOC) on the TP. In  
5 this study, we conducted multi-axis differential optical absorption spectroscopy (MAX-DOAS)  
6 measurements at Nam Co, the central TP, to observe the vertical profiles of aerosol, water vapor (H<sub>2</sub>O),  
7 NO<sub>2</sub>, HONO and O<sub>3</sub> from May to July 2019. In addition to NO<sub>2</sub> mainly exhibiting a Gaussian shape  
8 with the maximum value appearing at 300-400 m, other four species all showed an exponential shape  
9 and decreased with the increase of height. The maximum values of monthly averaged aerosol (0.17  
10 km<sup>-1</sup>) and O<sub>3</sub> (66.71 ppb) occurred on May, H<sub>2</sub>O ( $3.68 \times 10^{17}$  molec cm<sup>-3</sup>) and HONO (0.13 ppb)  
11 appeared on July, while NO<sub>2</sub> (0.39 ppb) occurred on June at 200-400 m layer. H<sub>2</sub>O, HONO and O<sub>3</sub> all  
12 exhibited a multi-peak pattern, and aerosol appeared a bi-peak pattern for their averaged diurnal  
13 variations. The averaged vertical profiles of OH production rates from O<sub>3</sub> and HONO all exhibited an  
14 exponential shape decreasing with the increase of height with maximum values of 2.61 ppb/h and 0.49  
15 ppb/h at the bottom layer, respectively. The total OH production rate contributed by HONO and O<sub>3</sub> on  
16 the TP was obviously larger than that in low-altitude areas. In addition, source analysis for HONO and  
17 O<sub>3</sub> at different height layers were conducted. The heterogeneous reaction of NO<sub>2</sub> on wet surfaces was a  
18 significant source of HONO. The maximum values of HONO/NO<sub>2</sub> appeared around H<sub>2</sub>O being  $1.0 \times$   
19  $10^{17}$  molec cm<sup>-3</sup> and aerosol being lager 0.15 km<sup>-1</sup> under 1.0 km, and the maximum values usually  
20 accompanied with H<sub>2</sub>O being  $1.0\text{-}2.0 \times 10^{17}$  molec cm<sup>-3</sup> and aerosol being lager 0.02 km<sup>-1</sup> at 1.0-2.0 km.  
21 O<sub>3</sub> was potentially sourced from south Asian subcontinent and Himalayas through long-range transport.  
22 Our results enrich the new understanding of vertical distribution of atmospheric components and  
23 explained the strong AOC on the TP.

## 25 1 Introduction

26 The TP spans 2.5 million square kilometers with an average altitude of over 4000 m. Therefore, the TP  
27 is called the “Third Pole” of the earth (Ma et al., 2020; Kang et al., 2022). It is the home to tens of  
28 thousands of glaciers and nourishes more than 10 of Asia’s rivers, thus it also acts the role of “Water  
29 Tower of Asia” (Qu et al., 2019; Ma et al., 2022). Due to its special topography, the TP is the heat  
30 source of atmosphere due the strong solar radiation, which as the driven force to profoundly affect the  
31 regional atmospheric circulation, global weather conditions and climate change (Yanai et al., 1992;  
32 Boos et al., 2010; Chen et al., 2015; Liu et al., 2022; Zhou et al., 2022). Monsoon rainfall in Asia, flood  
33 over the Yangtze River valley, and El Niño in the Pacific Ocean are strongly associated with the TP  
34 (Hsu et al., 2003; Li et al., 2016; Lei et al., 2019). In addition, the cyclone circulations caused by the  
35 TP heat source also can inhibit the diffusion of atmospheric pollutants in the areas around the TP, such  
36 as the Sichuan Basin, causing regional pollution (Zhang et al., 2019). Therefore, observations of the  
37 atmospheric species on the TP are essential to enhance the in-depth understanding of its atmospheric  
38 physicochemical processes.

39 However, deciphering the atmospheric environment of the TP is highly challenging and dangerous, due  
40 to its complex topography and harsh environment (Barnett et al., 2005; Bolch et al., 2012; Cong et al.,  
41 2015; Kang et al., 2016). In order to unveil the feature of atmospheric composition over the TP and  
42 their corresponding climate feedback, a large number of field observation stations have been  
43 established, and a series of field campaigns have continued to be carried out recently, especially after  
44 the performance of “the Second Tibetan Plateau Scientific Expedition and Research Program” (Che and  
45 Zhao 2021; Wang et al., 2021; Ran et al., 2022). The China National Environmental Monitoring Center  
46 (CNEMC) has established an in-situ monitoring network with more than 12 stations over the TP, such  
47 as Lhasa, Shigatse, Shannan, Nyingchi, Nagqu, Ngari, Qamdo, Diqing, Aba, Guoluo, Xining, and  
48 Haixi, to continuously monitor the surface concentrations of six atmospheric components (i.e. PM<sub>10</sub>,  
49 PM<sub>2.5</sub>, NO<sub>2</sub>, SO<sub>2</sub>, O<sub>3</sub> and CO) since 2013 (Gao et al., 2020; Li et al., 2020; Sun et al., 2021). The  
50 Institute of Tibetan Plateau Research, Chinese Academy of Sciences, has also established six long-term  
51 field observation stations to measure meteorological parameters and small amounts of atmospheric  
52 composition (i.e. black carbon, aerosol optical density (AOD)) (Ma et al., 2020). In addition, scientists  
53 are relying on advancements in satellite remote sensing technology, such as the tropospheric  
54 monitoring instrument (TROPOMI), the ozone monitoring instrument (OMI), the moderate-resolution  
55 imaging spectroradiometer (MODIS) and the cloud-aerosol lidar and infrared pathfinder satellite  
56 observation (CALIPSO), to monitor the spatial and temporal evolutions of atmospheric composition on  
57 the TP (Zhu et al., 2019; Li et al., 2020; Rawat and Naja 2022). Their advantage is to obtain the column  
58 densities of pollutants in a large-scale space of the TP. Although CALIPSO could detect aerosol  
59 vertical profiles, the spatiotemporal resolution (i.e. ~5.0 km horizontal resolution, 0.06 km vertical  
60 resolution and ~16 d temporal resolution) is limited and the data uncertainty in the planetary boundary  
61 layer (PBL) is large due to the low signal-to-noise ratio (Huang et al., 2007). However, several studies  
62 also revealed that the formation, aging and transport processes of atmospheric composition on the TP  
63 occurs not only near the ground surface but also at high altitudes (Xu et al., 2020; Xu et al., 2022). The  
64 high PBL on the TP caused by its strong solar radiation and undulating terrain promotes the  
65 atmospheric exchange between the bottom troposphere and stratosphere (Yang et al., 2003; Seidel et al.,  
66 2010). Therefore, the lack of vertical profiles of hinders the understanding of the evolution of trace  
67 gases and their environmental and climate effects over the TP. In recent years, balloon and lidar  
68 vertical measurements on the TP are occasionally carried out (Fang et al., 2019; Zhang et al., 2020;  
69 Dong et al., 2022), but their limited detection species (i.e. aerosol and O<sub>3</sub>) and high cost are obstacles  
70 that limit long-term continuous observation and the conduction of more in-depth scientific research.  
71 MAX-DOAS has the technical advantage of low-cost continuous observation of multiple atmospheric  
72 components (i.e. aerosol, O<sub>3</sub> and their precursors) (Wang et al., 2018; Ma et al., 2020; Cheng et al.,  
73 2021; Xing et al., 2021; Li et al., 2022; Cheng et al., 2023a, 2023b). Combining these data with better  
74 scientific models can reduce the modeling bias and promote to better understand the physical, chemical  
75 and dynamical processes.

76 The strong convergent airflow formed under the combined action of monsoon, subtropical anticyclone  
77 and the airflow of subtropical westerlies could promote the accumulation of O<sub>3</sub> on the TP in summer

78 (Ye and Gao 1997). Therefore, several studies have revealed the high O<sub>3</sub> concentration on the TP (Li et  
79 al., 2022; Yang et al., 2022; Yu et al., 2022). The strong solar radiation, high O<sub>3</sub> concentration and  
80 relatively high humidity on the TP provide great potential for high OH production. Lin et al. (2008) and  
81 Ye (2019) also confirmed that the high OH over the TP is mainly related to the reaction between O(<sup>1</sup>D)  
82 and H<sub>2</sub>O. The O(<sup>1</sup>D) is produced from the photolysis of O<sub>3</sub> by UV radiation. Therefore, a hypothesis of  
83 “strong AOC over the TP” was put forward. Previous studies pointed out that HONO also play an  
84 important role in AOC at low-altitude areas, and its contribution to OH can reach 40-60%, and even  
85 more than 80% in the early morning (Michoud et al., 2012; Ryan et al., 2018; Xue et al., 2020).  
86 However, few HONO studies on the TP have been reported. Our previous study operated at the  
87 Qomolangma Atmospheric and Environmental Observation and Research Station, Chinese Academy of  
88 Sciences (QOMS-CAS) revealed that the HONO mainly distributed in the lower PBL and peaked in  
89 summer with 1.11 ppb, which is comparable to the average level of HONO in other low-altitude areas  
90 (Luo et al., 2010; Xing et al., 2021a, 2021b; Yang et al., 2021). It indicates that it is also necessary to  
91 study the contribution of HONO to AOC on the TP. Furthermore, understanding the vertical  
92 distribution of OH is of great significance for learning about the atmospheric chemical processes and  
93 the evolution of atmospheric components on the TP (Zhou et al., 2015). Identifying the sources of O<sub>3</sub>  
94 and HONO is the basis for studying the AOC on the TP. The limited researches concluded that the  
95 atmospheric HONO on the TP is mainly sourced from the emissions of vehicles, biomass burning and  
96 soil, except for the NO<sub>2</sub> heterogeneous reaction on aerosol surfaces (Xing et al., 2021). The lower  
97 tropospheric O<sub>3</sub> on the TP is mainly dominated by local photochemical reactions, regional horizontal  
98 transport, vertical mixing and the intrusion from stratosphere (Yin et al., 2017; Xu et al. 2018).

99 In this study, we firstly analyzed the temporal and vertical characteristics of several atmospheric  
100 components (i.e. aerosol, H<sub>2</sub>O, NO<sub>2</sub>, HONO and O<sub>3</sub>) based on MAX-DOAS observations in Nam Co.  
101 Afterwards, the contributions of O<sub>3</sub> and HONO to OH in the vertical space were discussed through the  
102 tropospheric ultraviolet and visible (TUV) radiative transfer model and MAX-DOAS measurements.  
103 Finally, the potential sources of O<sub>3</sub> and HONO at different altitudes were analyzed based on the  
104 MAX-DOAS retrievals.

## 105 **2 Method and methodology**

### 106 **2.1 Site**

107 The Nam Co Monitoring and Research Station for Multisphere Interactions, CAS (NAMORS)  
108 (30.774°N, 90.988°E; 4730 m a.s.l.) is located at the southeast banks of Nam Co lake and the foothills  
109 of the northern Mt. Nyainqêntanglha (Fig. 1). The station land is covered by alpine meadows with soil  
110 type of sandy silt loam. The southwest monsoon can carry abundant moisture from Indian Ocean to this  
111 station in summer to increase humidity and precipitation there. Moreover, due to the summertime huge  
112 evaporation from Nam Co lake, the atmospheric H<sub>2</sub>O around CAS (NAMORS) is more abundant than  
113 in other areas of the TP, resulting in lush grass vegetation and making the area around this station an  
114 important summertime pasture. In addition, there are not large industries and cities within 100 km of  
115 the CAS (NAMORS). The closest town to CAS (NAMORS) is Dangxiong county which is about 60  
116 km away from this station and lower about 500 m than this station. Only a small number of vehicles  
117 pass through this area during summer tourism season. Therefore, no obvious anthropogenic sources of  
118 air pollutants exist near this station. Averaged spatial distributions of AOD, O<sub>3</sub>, NO<sub>2</sub> and HCHO  
119 monitored by satellite from May to July 2019 are shown in Figure S1. Elevated AOD, NO<sub>2</sub>, and O<sub>3</sub> are  
120 mainly distributed in South Asian subcontinent (e.g. India and Nepal), the southern foothills of the  
121 Himalayas, which is located in the upwind direction of the southwest monsoon potentially affecting the  
122 atmospheric composition over CAS (NAMORS).

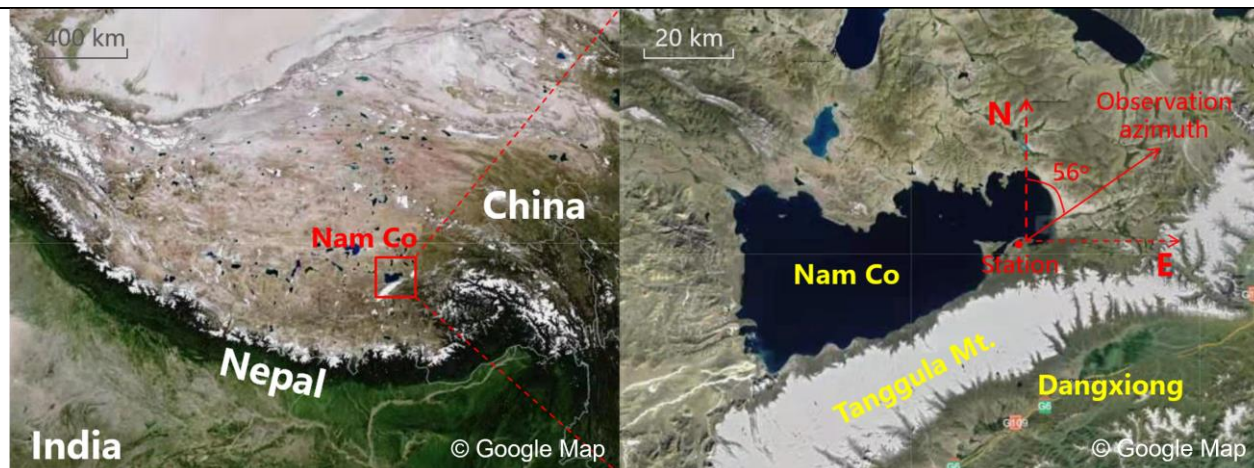


Figure 1. Geographical location of CAS (NAMORS) on the Tibet plateau.

## 2.2 Measurements

### 2.2.1 Instrument setup and spectral analysis

The MAX-DOAS instrument installed at CAS (NAMORS) was operated from 01 May to 09 July 2019. It consists of three major parts: telescope unit, spectrometer unit and control unit. The detailed description of this instrument can be found in Xing et al. (2021). In this study, the elevation angle sequence was set to 1, 2, 3, 4, 5, 6, 8, 10, 15, 30, and 90° with an exposure time of 60 s to each individual spectrum. The azimuth angle was set to 56° pointing to Nagqu direction. Moreover, only spectra collected under solar zenith angle (SZA) less than 75° was used for spectral analysis to avoid the strong stratospheric absorption.

The differential slant column densities (DSCDs) of O<sub>4</sub>, H<sub>2</sub>O, NO<sub>2</sub>, HONO and O<sub>3</sub> were retrieved using QDOAS software (<http://uvvis.aeronomie.be/software/QDOAS/>) developed by Royal Belgian Institute for Space Aeronomy (BIRA-IASB). The zenith spectrum measured at every sequence were selected as scan Fraunhofer reference spectrum. The retrieval configurations of O<sub>4</sub>, H<sub>2</sub>O, NO<sub>2</sub>, HONO and O<sub>3</sub> followed Xing et al. (2017), Lin et al. (2020), Xing et al. (2021), Wang et al. (2020) and Wang et al. (2018), respectively. The detailed DOAS fit settings of above five species were listed in Table 1. Corrected I<sub>0</sub> (Aliwell et al., 2002) was used in this study. Fig. 2 shows a typical DOAS retrieval example for above five species. DOAS fit results with root mean square (RMS) values larger than 5 × 10<sup>-4</sup>, 5 × 10<sup>-4</sup>, 5 × 10<sup>-4</sup>, 1 × 10<sup>-3</sup>, and 6 × 10<sup>-4</sup> for O<sub>4</sub>, H<sub>2</sub>O, NO<sub>2</sub>, HONO, and O<sub>3</sub>, respectively, were filtered out. In addition, we calculated color index (CI) to remove cloud effect (Wagner et al., 2016). The data filter criteria according to CI followed by Ryan et al. (2018) and Xing et al. (2020). Afterwards, the quantified DSCDs of O<sub>4</sub>, H<sub>2</sub>O, NO<sub>2</sub>, HONO, and O<sub>3</sub> remained 91.33%, 91.97%, 92.16%, 86.42% and 81.09%, respectively.

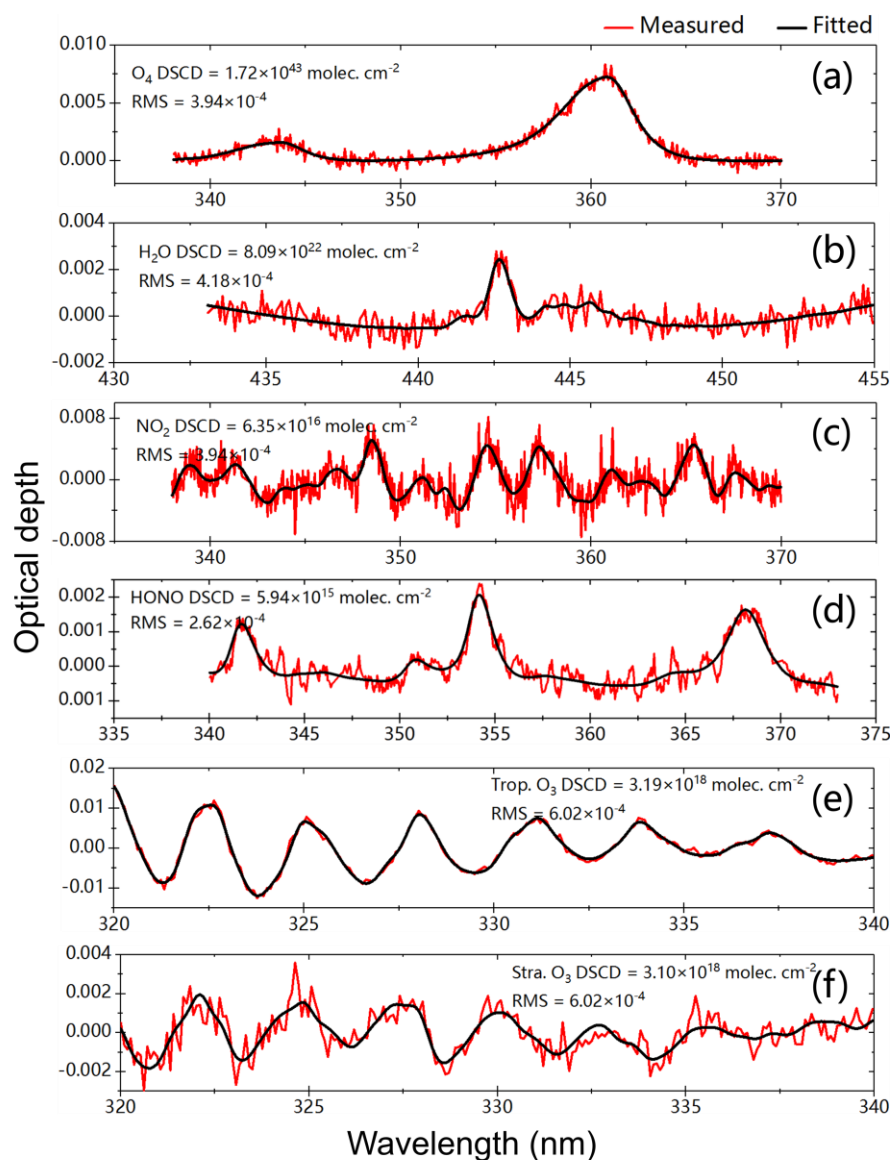
### 2.2.2 Vertical profile retrieval

The vertical profiles of aerosol and trace gases (i.e. H<sub>2</sub>O, NO<sub>2</sub>, HONO and O<sub>3</sub>) were retrieved using algorithm based on optimal estimation method (OEM). A linearized pseudo-spherical vector discrete ordinate radiative transfer model VLIDORT was used as forward model and a Gauss-Newton (GN) scheme was used as the inversion strategy (Wedderburn et al., 1974). The detailed description of this algorithm can be found in Liu et al. (2021), Xing et al. (2021) and Wang et al. (2018). The detailed retrieval processes were depicted in Sect. S1 of the supplement. In this study, the initial a priori profile shape of above five species was set to exponential decreasing shape, and the AOD and vertical column densities (VCDs) simulated by weather research and forecasting model coupled chemistry (WRF-Chem) were also used as initial input a priori information to constrain the retrieval process. For the O<sub>3</sub> profile retrieval, the stratospheric O<sub>3</sub> profile was deducted using TROPOMI O<sub>3</sub> profile (Zhao et al., 2021). We set 20 vertical layers from 0.0 to 4.0 km with a vertical resolution of 0.2 km. The correlation height was set to 1.0 km. Moreover, the surface albedo, single scattering albedo and asymmetry parameter were set to fixed constant of 0.08, 0.85 and 0.65, respectively (Irie et al., 2008). The retrieved vertical profiles

161 were removed under the condition of degree of freedom (DOF) and relative error less than 1.0 and  
 162 100%, respectively.

163 Table 1. Detailed DOAS retrieval settings for O<sub>4</sub>, H<sub>2</sub>O, NO<sub>2</sub>, HONO and O<sub>3</sub>.

Parameter	Data source	Fitting intervals (nm)				
		O <sub>4</sub>	H <sub>2</sub> O	NO <sub>2</sub>	HONO	O <sub>3</sub>
Wavelength range		338-370	433-455	338-370	340-373	320-340
NO <sub>2</sub>	298K, I <sub>0</sub> -corrected, Vandaele et al. (1998)	✓	✓	✓	✓	✓
NO <sub>2</sub>	220K, I <sub>0</sub> -corrected, Vandaele et al. (1998)	✓	✓	✓	✓	×
O <sub>3</sub>	223K, I <sub>0</sub> -corrected, Serdyuchenko et al. (2014)	✓	✓	✓	✓	✓
O <sub>3</sub>	243K, I <sub>0</sub> -corrected, Serdyuchenko et al. (2014)	✓	×	✓	✓	×
O <sub>3</sub>	293K, I <sub>0</sub> -corrected, Serdyuchenko et al. (2014)	×	×	×	×	✓
O <sub>4</sub>	293K, Thalman and Volkamer (2013)	✓	✓	✓	✓	✓
HCHO	298K, Meller and Moortgat (2000)	✓	×	✓	✓	✓
Glyoxal	298K, Volkamer (2005)	×	✓	×	×	×
H <sub>2</sub> O	HITEMP (Rothman et al. 2010)	✓	✓	✓	✓	×
BrO	223K, Fleischmann et al. (2004)	✓	×	✓	✓	×
HONO	296K, Stutz et al. (2000)	×	×	×	✓	×
Ring	Calculated with QDOAS	✓	✓	✓	✓	✓
Polynomial degree		Order 3	Order 3	Order 3	Order 5	Order 3
Intensity offset		Constant	Constant	Constant	Constant	No



164

165 Figure 2. DOAS fit examples of O<sub>4</sub>, H<sub>2</sub>O, NO<sub>2</sub>, HCHO, tropospheric O<sub>3</sub> and stratospheric O<sub>3</sub>. The red  
 166 line and black line represent the measured and fitted results, respectively.

### 167 2.2.3 Error analysis

168 The error sources can be divided into four different types: smoothing error, noise error, forward model  
 169 error, and model parameter error (Rodgers, 2004). However, in terms of this classification, some errors  
 170 are difficult to be calculated or estimated. For example, the forward model error, which is caused by an  
 171 imperfect representation of the physics of the system, is hard to be quantified due to the difficulty of  
 172 acquiring an improved forward model. Given calculation convenience and contributing ratios of  
 173 different errors in total error budget, we mainly took into account following error sources, which were  
 174 smoothing and noise errors, algorithm error, cross section error, and uncertainty related to the aerosol  
 175 retrieval (only for trace gas). In this study, we estimated the contribution of different error sources to  
 176 the AOD and VCDs of trace gases, and near-surface (0–200 m) trace gases' concentrations and aerosol  
 177 extinction coefficients (AECs), respectively. The detailed demonstrations and estimation methods are  
 178 displayed below.

- 179 a. Smoothing errors arise from the limited vertical resolution of profile retrieval. Noise errors denote  
 180 the noise in the spectra (i.e., the error of DOAS fits). Considering the error of the retrieved state  
 181 vector equaling the sum of these two independent errors, we calculated the sum of smoothing and  
 182 noise errors on near-surface concentrations and column densities, which were 13 and 5 % for  
 183 aerosols, 13 and 36 % for H<sub>2</sub>O, 12 and 14 % for NO<sub>2</sub>, 18 and 21 % for HONO, and 12 and 32 % for  
 184 O<sub>3</sub>, respectively.
- 185 b. Algorithm error is denoted by the differences between the measured and simulated DSCDs. This  
 186 error contains forward model error from an imperfect approximation of forward function, parameter  
 187 error of forward model, and other errors, such as detector noise (Rodgers, 2004). Algorithm error is  
 188 a function of the viewing angle, and it is difficult to assign this error to each altitude. Thus, this  
 189 error on the near-surface values and column densities is estimated through calculating the average  
 190 relative differences between the measured and simulated DSCDs at the minimum and maximum  
 191 elevation angle (except 90°), respectively (Wagner et al., 2004). In this study, we estimated these  
 192 errors on the near-surface values and the column densities at 4 and 8 % for aerosols, 3 and 11 % for  
 193 NO<sub>2</sub>, and 20 and 20 % for HONO referring to Wang et al. (2017, 2020), 1 and 8 % for H<sub>2</sub>O  
 194 referring to Lin et al. (2020), and 6 and 10 % for O<sub>3</sub> referring to Ji et al. (2023), respectively.
- 195 c. Cross section error arises from the uncertainty in the cross section. According to Thalman and  
 196 Volkamer, (2013), Lin et al. (2020), Vandaele et al. (1998), Stutz et al. (2000), and Serdyuchenko  
 197 et al. (2014), we adopted 4, 3, 3, 5, and 2 % for O<sub>4</sub> (aerosols), H<sub>2</sub>O, NO<sub>2</sub>, HONO and O<sub>3</sub>,  
 198 respectively.
- 199 d. The profile retrieval error for trace gases is sourced from the uncertainty of aerosol extinction  
 200 profile retrieval and propagated to trace gas profile. This error could be roughly estimated based on  
 201 a linear propagation of the total error budgets of the aerosol retrievals. The errors of the learned  
 202 four trace gases were roughly estimated at 14 % for VCDs and 10 % for near-surface  
 203 concentrations, respectively.

204 The total uncertainty was the sum of all above errors in the Gaussian error propagation, and the error  
 205 results were listed in Table 2. We found that the smoothing and noise errors played a dominant role in  
 206 the total uncertainties of aerosol and trace gases. Moreover, improving the accuracy and temperature  
 207 gradient of the absorption cross section is another important means to reduce the uncertainty of the  
 208 vertical profiles in the future, especially for O<sub>3</sub>.

209 Table 2. Error budget estimation (in %) of the retrieved near-surface (0–200 m) concentrations of trace  
 210 gases and AECs, and AOD and VCDs.

		Error sources				Total
		Smoothing and noise errors	Algorithm error	Cross section error	Related to the aerosol retrieval	
Near-surface	aerosol	13	4	4	/	14
	H <sub>2</sub> O	13	1	3	14	19
	NO <sub>2</sub>	12	3	3	14	18
	HONO	18	20	5	14	29



	O <sub>3</sub>	12	6	2	14	19
VCD or AOD	AOD	5	8	4	/	10
	H <sub>2</sub> O	36	8	3	10	38
	NO <sub>2</sub>	14	11	3	10	20
	HONO	21	20	5	10	31
	O <sub>3</sub>	32	10	2	10	35

211

## 212 **2.3 TUV model**

213 The calculation of photolysis rates of HONO and O<sub>3</sub> used TUV radiation model  
 214 (<https://www2.acom.ucar.edu/modeling/tropospheric-ultraviolet-and-visible-tuv-radiation-model>)  
 215 based on a full FORTRAN code. In order to ensure the accuracy of model running, we only selected  
 216 data in sunny and cloudless days. Moreover, we developed a cloud classification method based on the  
 217 diurnal variations of Color Index (CI=I<sub>330</sub>/I<sub>360</sub>) in Figure S2. The initial input parameters were as  
 218 follows: the AOD at 361 nm was derived from aerosol extinction profiles measured by MAX-DOAS;  
 219 the daily total ozone column density was measured by TROPOMI with a value range of 260-280 DU;  
 220 the single scattering albedo (SSA) was calculated based on the regression analysis of multi-wavelength  
 221 (361 and 477 nm) O<sub>4</sub> absorptions measured by MAX-DOAS (Xing et al., 2019); fixed Ångström  
 222 exponents of 0.508, 0.581 and 0.713 were used in May, June and July, respectively, referring to Xia et  
 223 al. (2011).

## 224 **2.4 Backward trajectory, PSCF and CWT analysis**

225 The 48-h backward trajectories at five heights of 200, 600, 1000, 1400 and 1800 m were calculated  
 226 using the Hybrid Single-particle Lagrangian Integrated Trajectory (HYSPLIT) model based on the  
 227 Global Data Assimilation System (GDAS) to identify the major transport pathways of O<sub>3</sub> (Draxler and  
 228 Hess, 1998). Moreover, the calculated backward trajectories were clustered into three groups using  
 229 Ward's variance method and Angle Distance algorithm (Ward 1963; Wang et al., 2006).

230 In order to determine the potential source locations of O<sub>3</sub> over CAS (NAMORS), the Potential Source  
 231 Contribution Function (PSCF) model and Concentration Weighted Trajectory (CWT) model were used  
 232 (Hong et al., 2019; Ou et al., 2021). The PSCF was calculated through the number of air trajectory  
 233 endpoints being divided by the number of air trajectory endpoints. Moreover, a weighting function was  
 234 introduced to reduce the increased uncertainties of PSCF with the increase of the distance between the  
 235 grid and sampling point. In this study, the set of this weighting function referred to Yin et al. (2017).  
 236 CWT can be used to calculate the weight concentration through averaging the concentrations  
 237 associated with trajectories crossing the grid cell. Above weighting function was also introduced to  
 238 calculate the WCWT (Hsu, et al., 2003). The detailed description of these two models can be found in  
 239 Wang et al., 2006.

## 240 **2.5 Ancillary data**

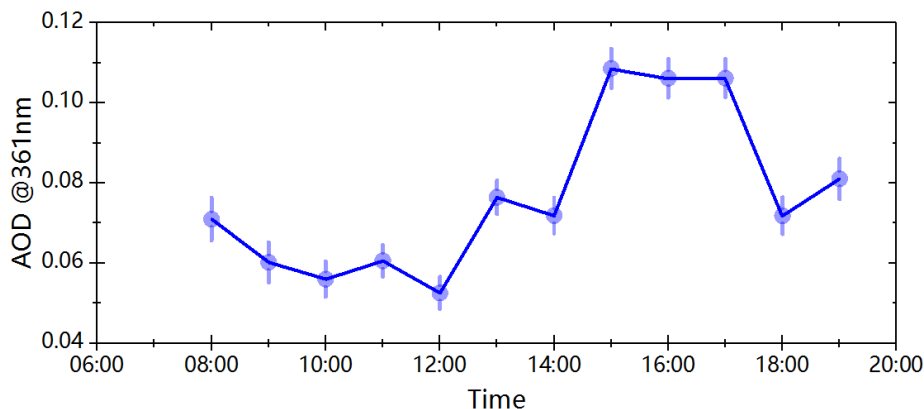
241 The surface NO<sub>2</sub>, HONO and O<sub>3</sub> concentrations used to validate the corresponding MAX-DOAS  
 242 measurements were monitored by broadband cavity enhanced spectrometer (BBCES) (Fang et al.,  
 243 2017), long path absorption photometer (LOPAP) (Kleffmann et al., 2008) and Thermo Electron 49i  
 244 (Shi et al., 2009), respectively. The PBL height was simulated using WRF with spatiotemporal  
 245 resolutions of 20×20 km<sup>2</sup> and 1.0 hour (detailed configurations in Sect. S3 of the supplement).  
 246 Moreover, the large-scaled spatial distributions of AOD, O<sub>3</sub> and NO<sub>2</sub> over CAS (NAMORS) were  
 247 monitored by Himawari-8 (Bessho et al., 2016), OMI (Veefkind et al., 2004) and TROPOMI (Griffin et  
 248 al., 2018; Su et al., 2020), respectively.

## 249 **3 Results**

### 250 **3.1 Overview of the measurements**

251 Figure 3 showed the averaged diurnal variation of AOD from 1<sup>st</sup> May to 9<sup>th</sup> July 2019, with an average  
 252 value of 0.076 km<sup>-1</sup> during 08:00-19:00. The AOD was 0.071 km<sup>-1</sup> at 08:00, and then gradually  
 253 decreased to a minimum value of 0.052 km<sup>-1</sup> at 12:00. Subsequently, the AOD increased significantly,

254 reaching maximum values during 15:00-17:00 (average of  $0.107\text{km}^{-1}$ ), which was about 1.408 times  
 255 the diurnal average value. Considering the diurnal variation of wind speed (Figure S3), such an  
 256 enhancement of AOD may be related to the long-range transport of aerosol from southern Asia (Yang  
 257 et al., 2020; Bi et al., 2023). Moreover, 15:00-17:00 was the active time of tourists and local residents  
 258 (i.e. cooking), and these kinds of anthropogenic sources contributed to the atmospheric AOD of  
 259 NAMORS through short-distance transport (Yin et al., 2017; Zhang et al., 2017). After 17:00, the  
 260 AODs decreased rapidly to  $0.071\text{ km}^{-1}$  at 18:00 and  $0.081\text{ km}^{-1}$  at 19:00, respectively.



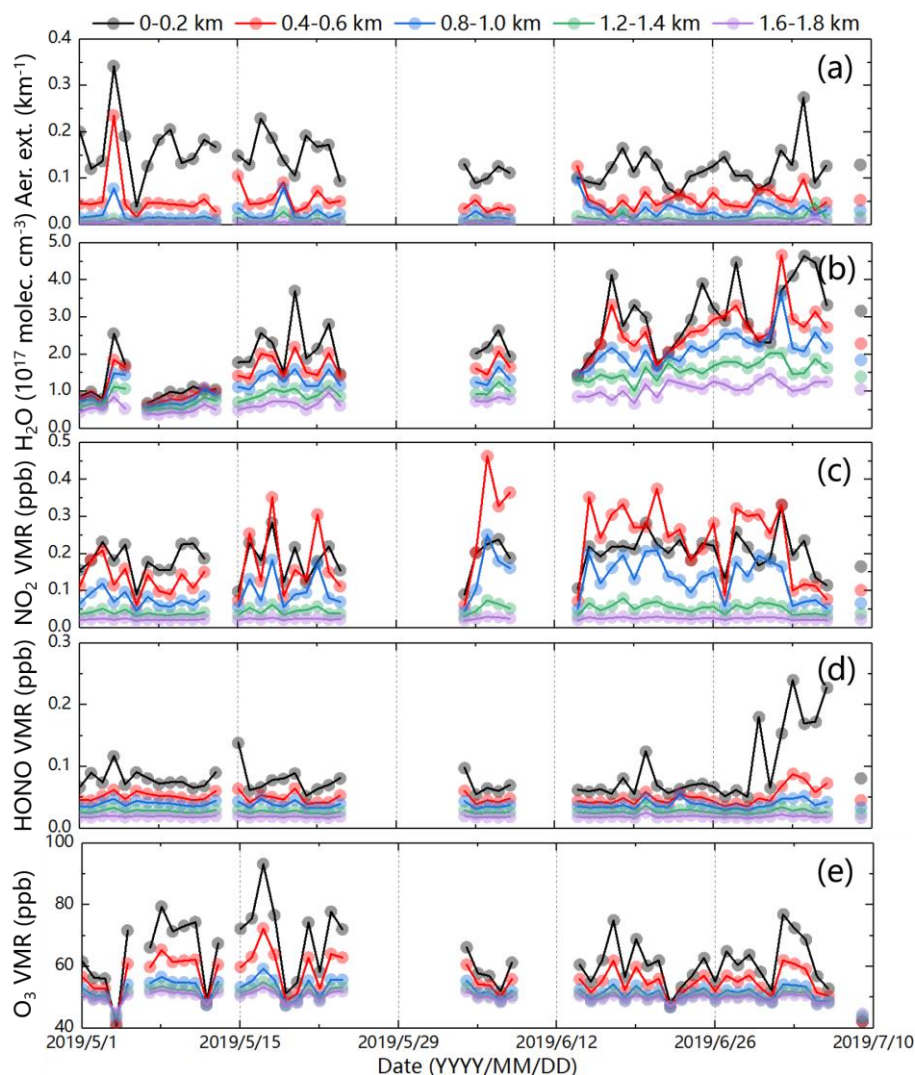
261  
 262 Figure 3. Averaged diurnal variation of AOD at CAS (NAMORS). The error bars represent the mean retrieved errors  
 263 of AOD.

264 As shown in Figure S4, the diurnal variation of PBL in Nam Co from May to July 2019 was lower in  
 265 the early morning and late afternoon, but higher between 11:00 and 17:00, a relatively long period,  
 266 with the maximum PBL larger than 2.0 km. Zhang et al. (2017) and Yang et al., (2017) also reported  
 267 that the PBL in Nam Co was usually larger than 1.0 km during daytime in spring and summer. In order  
 268 to investigate the height-dependent variations of aerosol,  $\text{H}_2\text{O}$ ,  $\text{NO}_2$ , HONO and  $\text{O}_3$  within the PBL  
 269 during the measurements, five height layers under the PBL (0.0-0.2 km, 0.4-0.6 km, 0.8-1.0 km,  
 270 1.2-1.4 km and 1.6-1.8 km) were thus selected.

271 Figure 4 showed the time series of the daily averaged aerosol,  $\text{H}_2\text{O}$ ,  $\text{NO}_2$ , HONO and  $\text{O}_3$  at above five  
 272 layers from 1<sup>st</sup> May to 9<sup>th</sup> July 2019. Aerosol mainly distributed at 0.0-0.2 km with an average  
 273 extinction coefficient of  $0.138\text{ km}^{-1}$ , and the ratios of aerosol extinction at 0.4-0.6 km, 0.8-1.0 km,  
 274 1.2-1.4 km and 1.6-1.8 km to those at 0.0-0.2 km were 39.34%, 18.77%, 7.29% and 2.62%,  
 275 respectively. That indicated that the aerosol was usually local-emitted at the surface, and the  
 276 occasionally appearance of strong aerosol extinction at 0.4-0.6 km, such as 13<sup>th</sup> and 30<sup>th</sup> June, was  
 277 associated with long-range transport from south Asia (Figure S5, Wan et al., 2015; Li et al., 2016). The  
 278 average concentration of  $\text{H}_2\text{O}$  at 0.0-0.2 km was  $2.35 \times 10^{17}\text{ molec cm}^{-3}$ , and the ratios of  $\text{H}_2\text{O}$  at  
 279 0.4-0.6 km, 0.8-1.0 km, 1.2-1.4 km and 1.6-1.8 km to those at 0.0-0.2 km were 83.40%, 68.08%,  
 280 50.64% and 35.74%, respectively, which should attribute to the transport of  $\text{H}_2\text{O}$  from southern Asia  
 281 driven by the Indian ocean monsoon and the elevated evaporation from Nam Co lake to lead to its not  
 282 obvious vertical gradient (Figure S6, Lei et al., 2014; Zhu et al., 2019). The average concentration of  
 283  $\text{NO}_2$  at 0.0-0.2 km was 0.193 ppb, and its high concentration mainly distributed at 0.4-0.6 km after 15<sup>th</sup>  
 284 May. The ratios of  $\text{NO}_2$  at 0.4-0.6 km, 0.8-1.0 km, 1.2-1.4 km and 1.6-1.8 km to those at the bottom  
 285 layer were 104.03%, 59.05%, 24.62% and 12.84%, respectively. The elevation of the distribution  
 286 height of high concentration  $\text{NO}_2$  should be attributed to the transport process from the  $\text{NO}_x$  produced  
 287 by ice and snow on the top of Mt. Tanggula under strong ultraviolet radiation (Boxe et al., 2005; Fisher  
 288 2005; Lin et al., 2021). As depicted in Figure S7, the WPCF passing through Mt. Tanggula showed  
 289 high values at 300-400 m layer, especially at 400 m ( $> 0.3$ ). It also indirectly indicated that the  
 290 important contribution to  $\text{NO}_x$  from ice and snow on the top of mountains under strong ultraviolet  
 291 radiation on the TP. HONO mainly distributed at 0.0-0.2 km with an average value of 0.087 ppb, and  
 292 the ratios of HONO at 0.4-0.6 km, 0.8-1.0 km, 1.2-1.4 km and 1.6-1.8 km to those at 0.0-0.2 km were  
 293 58.49%, 44.64%, 31.30% and 21.67%, respectively. That indicated that the primary and secondary  
 294 sources of HONO were mainly at the surface (Section 4.2). The vertical gradient of daily averaged  $\text{O}_3$   
 295 concentration was also not obvious, which was associated with its vertical mixing and photochemical



296 production (Yin et al., 2017). As shown in Figure S8, the corresponding TROPOMI O<sub>3</sub> profiles in Nam  
 297 Co and O<sub>3</sub> profiles measured by lidar and ozonesonde around Nam Co reported in several previous  
 298 studies also exhibited an exponential shape (Fang et al., 2019; Zhang et al., 2020; Yu et al., 2022). The  
 299 O<sub>3</sub> average concentration at 0.0-0.2 km was 63.030 ppb, and the ratios of O<sub>3</sub> at 0.4-0.6 km, 0.8-1.0 km,  
 300 1.2-1.4 km and 1.6-1.8 km to those at surface were 89.25%, 82.44%, 80.16% and 79.13%, respectively.

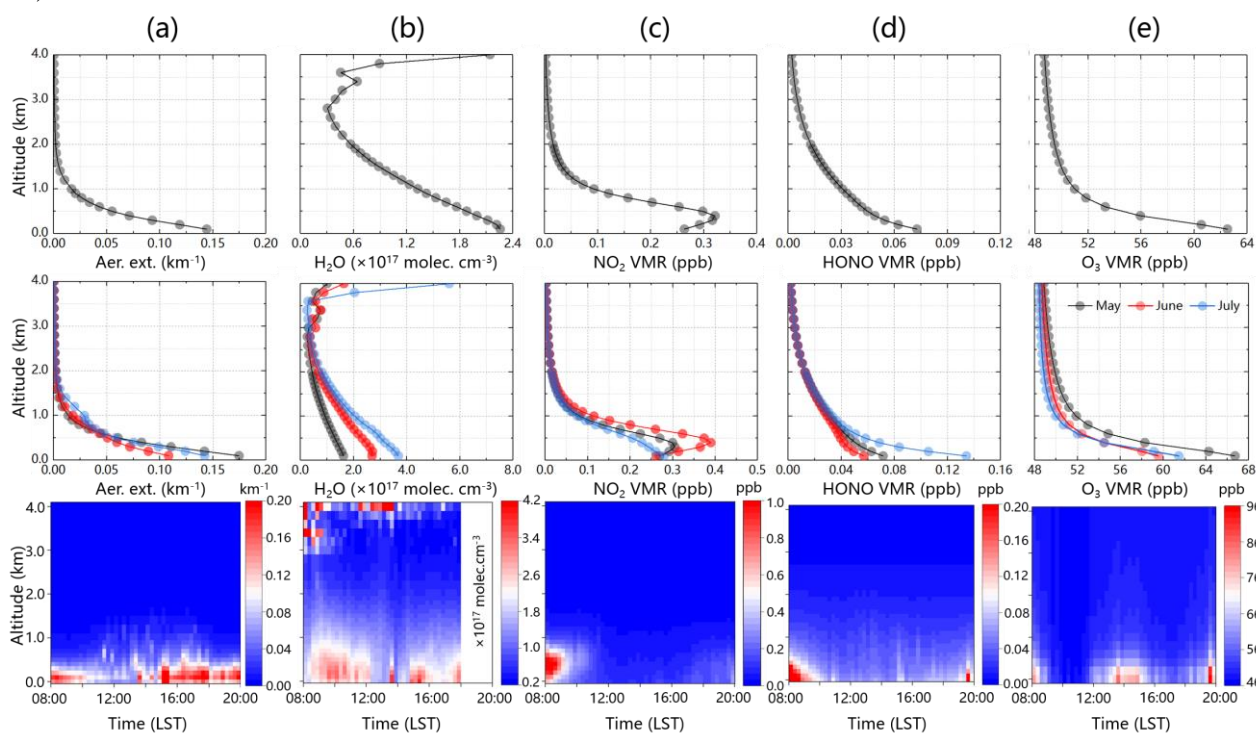


301  
 302 Figure 4. Time series of daily averaged (a) aerosol extinction, (b) H<sub>2</sub>O, (c) NO<sub>2</sub>, (d) HONO, and (e) O<sub>3</sub>  
 303 monitored by MAX-DOAS at 0-0.2, 0.4-0.6, 0.8-1.0, 1.2-1.4 and 1.6-1.8 km five height layers from 01  
 304 May to 09 July 2019.

### 305 3.2 Vertical distributions of aerosol, H<sub>2</sub>O, NO<sub>2</sub>, HONO and O<sub>3</sub>

306 The first row in Figure 5 provided the averaged vertical profiles of aerosol, H<sub>2</sub>O, NO<sub>2</sub>, HONO and O<sub>3</sub>  
 307 from May to July 2019. We found that the vertical profiles of aerosol, H<sub>2</sub>O, HONO and O<sub>3</sub> all  
 308 exhibited an exponential shape with maximum values near the surface, while NO<sub>2</sub> exhibited a Gaussian  
 309 shape with the maximum value of 0.321 ppb occurring at 0.3-0.4 km layer. In addition to the effect of  
 310 NO<sub>x</sub> transport, Xu et al. (2018) also revealed that the long-range high-altitude transport process from  
 311 the northern south Asian subcontinent can significantly enhance the Nam Co's peroxyacetyl nitrate  
 312 (PAN) level which is a reservoir of NO<sub>x</sub>. As shown in the second row of Figure 5, the monthly  
 313 averaged aerosol vertical profiles from May to July 2019 all exhibited an exponential shape, and varied  
 314 in the order of May (0.17 km<sup>-1</sup>) > July (0.14 km<sup>-1</sup>) > June (0.11 km<sup>-1</sup>). Xu et al. (2018) and Neupane et  
 315 al. (2019) also reported a similar monthly variations of black carbon (BC) from May to July over the  
 316 TP, and revealed that it was mainly associated with the anthropogenic emissions (i.e. biomass burning)  
 317 and its transport from south Asia. The monthly averaged vertical profile of H<sub>2</sub>O in May and July  
 318 exhibited an exponential shape, while its maximum concentration layer slightly elevated to 0.1-0.2 km

319 in June which was related to the strongest monsoon transport (Figure S9). It varied in the order of July  
 320 ( $3.68 \times 10^{17}$  molec  $\text{cm}^{-3}$ ) > June ( $2.71 \times 10^{17}$  molec  $\text{cm}^{-3}$ ) > May ( $2.26 \times 10^{17}$  molec  $\text{cm}^{-3}$ ), and its  
 321 maximum concentration occurring in July was strongly associated with the enhanced evaporation from  
 322 the Nam Co lake (Xu et al., 2011). The monthly averaged vertical profiles of  $\text{NO}_2$  all exhibited a  
 323 Gaussian shape from May to July, and its maximum values mainly distributed at 0.2-0.4 km layer  
 324 varying in the order of June (0.39 ppb) > May (0.31 ppb) > July (0.28 ppb). It indicated that the  
 325 regional transport from the  $\text{NO}_x$  produced from ice and snow under strong shortwave radiation (Figure  
 326 S7),  $\text{NO}_2$  emitted from vehicles due to the increased tourism, anthropogenic emissions from local  
 327 residents (i.e. biomass burning and religious activities) played an important role in the vertical  
 328 distribution characteristic of  $\text{NO}_2$  (Boxe et al., 2005; Chen et al., 2019). The monthly averaged vertical  
 329 profiles of HONO from May to July all exhibited an exponential shape, with maximum values near the  
 330 surface varying in the order of July (0.13 ppb) > May (0.07 ppb) > June (0.06 ppb). The local direct  
 331 emissions from biomass burning, vehicles and soil should be main sources of the surface HONO (Xing  
 332 et al., 2021). Moreover, the heterogeneous reaction of  $\text{NO}_2$  on wet surfaces should be another important  
 333 source of HONO at different height layers (Section 4.2). For example, the aerosol extinction coefficient,  
 334 and the concentrations of  $\text{H}_2\text{O}$  and  $\text{NO}_2$  were all relatively large at the bottom layer in July,  
 335 correspondingly, we observed the highest concentration of HONO near the surface in this month. The  
 336 monthly averaged  $\text{O}_3$  vertical profiles all showed an exponential shape from May to July, and its  
 337 surface concentration varied in the order of May (66.71 ppb) > July (61.45 ppb) > June (59.55 ppb).  
 338 This kind of monthly variation trend of  $\text{O}_3$  was also reported by several previous studies (Yin et al.,  
 339 2017; Xu et al., 2018). The  $\text{O}_3$  in Nam Co was mainly sourced from stratospheric intrusion,  
 340 photochemical reactions, long-range transport and local vertical mixing (Yin et al., 2017; Chen et al.,  
 341 2019).



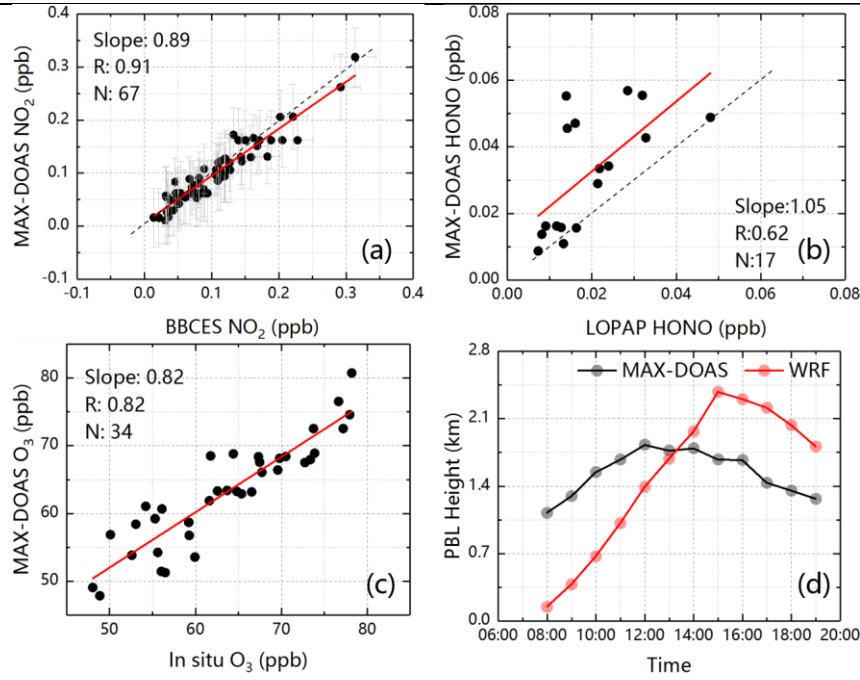
342  
 343 Figure 5. Vertical profiles of (a) aerosol extinction, (b)  $\text{H}_2\text{O}$ , (c)  $\text{NO}_2$ , (d) HONO, and (e)  $\text{O}_3$ . The top  
 344 row shows the averaged vertical profiles from 01 May to 09 July 2019. The middle row shows the  
 345 monthly averaged vertical profiles. The bottom row shows the averaged diurnal vertical profiles from  
 346 01 May to 09 July 2019.

347 The third row in Figure 5 illustrated the averaged diurnal variations in vertical profiles of aerosol,  $\text{H}_2\text{O}$ ,  
 348  $\text{NO}_2$ , HONO and  $\text{O}_3$  from May to July 2019. Aerosol mainly distributed under 1.0 km, especially 0.6  
 349 km, and its mixing height was gradually increased with the rise of the PBL height after 12:00.  
 350 Moreover, the diurnal variation of aerosol showed a bi-peak pattern, which was in line with the  
 351 investigation reported by Pokharel et al. (2019). The first peak occurred between 08:00-10:00, and

352 another appeared after 15:00. The first peak should be attributed to the local emission of aerosol and  
353 the diurnal cycle of PBL (Zhang et al., 2017; Pokharel et al., 2019). The second peak was driven by  
354 regional transport and the interaction between local sandy silt loam surface and local meteorology. The  
355 high wind speed ( $> 4.5$  m/s) at surface appeared after 15:00, which coincided with the appearance of  
356 the second aerosol peak (Figure S3). Moreover, the high extinction during the second peak was  
357 extended to 1.0 km associated with the wind speed larger than 8 m/s (Figure S10), which created a  
358 favorable condition for high-altitude aerosol transport.  $\text{H}_2\text{O}$  mainly distributed under 1.0 km and above  
359 3.0 km, and its diurnal variation exhibited a multi-peak pattern. The first peak appeared between  
360 08:00-12:00, which was mainly affected by the monsoon driven long-range transport of  $\text{H}_2\text{O}$  (Cong et  
361 al., 2009; Xu et al., 2020). The second and third peaks occurred at 15:00-16:00 and after 17:00,  
362 respectively. In addition to long-range transport, the enhanced evaporation from the Nam Co lake also  
363 significantly contributed to the appearance of these two peaks of  $\text{H}_2\text{O}$  (Xu et al., 2011).  $\text{NO}_2$  mainly  
364 distributed at 0.2-0.4 km, and peaked before 10:00 and after 18:00 which were dominated by the effects  
365 of local emissions and regional transport from the  $\text{NO}_x$  formed through ice and snow on the top of Mt.  
366 Tanggula under strong ultraviolet radiation (Figure S7) (Boxe et al., 2005; Fisher 2005; Chen et al.,  
367 2019; Lin et al., 2021). Moreover, its diurnal mixing height was obviously correlated to the diurnal  
368 evolution of PBL height. HONO mainly distributed under 1.0 km, especially 0.4 km. Its diurnal  
369 variation showed a multi-peak pattern with three obvious peaks before 10:00, 15:00-16:00, and after  
370 19:00. In addition to local emissions (i.e. vehicle emission, biomass burning and soil emission), the  
371 heterogeneous reaction of  $\text{NO}_2$  on wet surfaces should be also an important HONO source (Xing et al.,  
372 2021). We found that there were larger aerosol extinction ( $> 0.12 \text{ km}^{-1}$ ) and higher concentrations of  
373  $\text{NO}_2$  ( $> 0.20$  ppb) and  $\text{H}_2\text{O}$  ( $> 2.27 \times 10^{17} \text{ molec cm}^{-3}$ ) around three HONO peaks.  $\text{O}_3$  mainly  
374 distributed under 0.4 km, and its diurnal variation exhibited a multi-peak pattern with three peaks  
375 appearing before 09:00, 13:00-15:00 and after 19:00. The appearance of  $\text{O}_3$  peaks was mainly  
376 associated with the influence of the complex topography of the TP, long-range transport, local vertical  
377 mixing and stratospheric intrusion (Yin et al., 2017; Chen et al., 2019; Qian et al., 2022). The active  
378 photochemical reaction should be another important source of  $\text{O}_3$ , especially for its second peak at  
379 13:00-15:00.

### 380 **3.3 Validation with independent data**

381 In order to validate the MAX-DOAS dataset, we extracted the concentrations of  $\text{NO}_2$ , HONO and  $\text{O}_3$  at  
382 the bottom layer (0.0-0.1 km) from their corresponding vertical profiles to compare with in situ  
383 measurements. As shown in Figure 6(a-c), we found good agreements between MAX-DOAS and in  
384 situ observations with Pearson correlation coefficients (R) of 0.91, 0.62 and 0.82 (regression slope of  
385 0.89, 1.05 and 0.82) for  $\text{NO}_2$ , HONO and  $\text{O}_3$ , respectively. That indicated the good reliability of trace  
386 gases from MAX-DOAS retrievals. Moreover, we also compared the MAX-DOAS PBL and WRF PBL,  
387 and a similar variation trend was found. However, WRF PBL showed a significantly difference in  
388 height values with MAX-DOAS PBL before 12:00. That should be due to the simulation uncertainties  
389 for WRF model at Tibetan plateau with complex topography and meteorology (Yang et al., 2016; Xu et  
390 al., 2019).



391

392 Figure 6. Validations of (a) MAX-DOAS NO<sub>2</sub> vs in situ NO<sub>2</sub> (error bars represent the retrieved errors  
 393 of NO<sub>2</sub> from MAX-DOAS and BBCES), (b) MAX-DOAS HONO vs LOPAP HONO, (c)  
 394 MAX-DOAS O<sub>3</sub> vs in situ O<sub>3</sub>, and (d) MAX-DOAS PBL vs WRF PBL.

## 395 4 Discussion

### 396 4.1 OH production

397 HONO and O<sub>3</sub> are two important precursors of OH radical to enhance the AOC (Kleffmann et al., 2005;  
 398 Ryan et al., 2018; Xing et al., 2021). In order to evaluate the AOC on the TP, we tried to analyze the  
 399 OH production from HONO and O<sub>3</sub> at different height layers through vertical observations and TUV  
 400 calculations. The OH production rates from HONO and O<sub>3</sub> were calculated using the following two  
 401 equations:

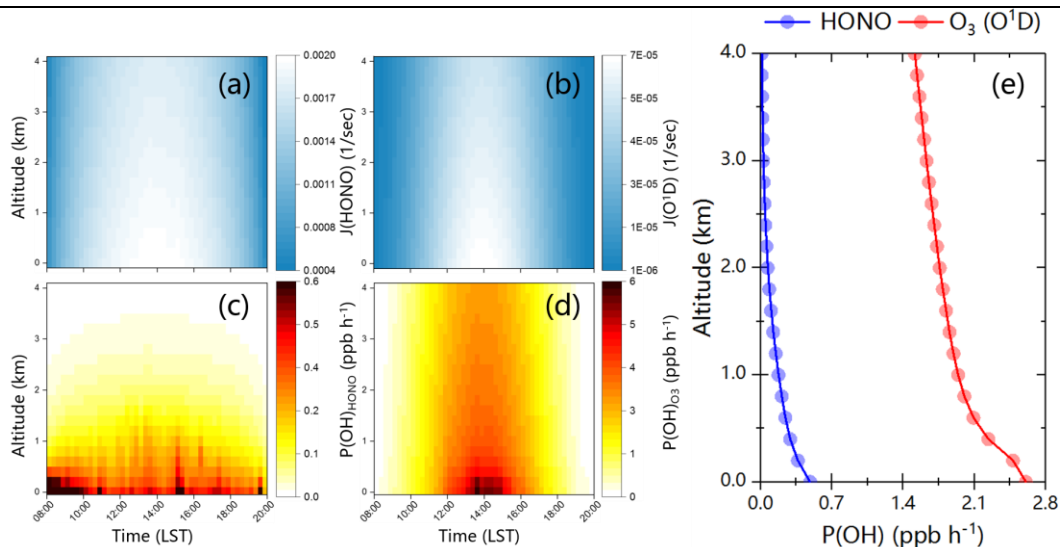
$$402 P(OH)_{HONO} = J(HONO) \times [HONO]$$

$$403 P(OH)_{O_3} = 2 \times f \times J(O(^1D)) \times [O_3]$$

404 Where  $J(HONO)$  and  $J(O(^1D))$  were the photolysis rates of HONO and O(<sup>1</sup>D) calculated using TUV  
 405 model. O(<sup>1</sup>D) was the product from O<sub>3</sub> photolysis by UV radiation.  $f$  was the fraction of the process  
 406  $O(^1D) + H_2O \rightarrow 2OH$ .

407 Figure 7(a-b) showed the averaged diurnal vertical distributions of the photolysis rates  $J(HONO)$  and  
 408  $J(O(^1D))$  from May to July 2019. We found that the maximum  $J(HONO)$  and  $J(O(^1D))$  were all  
 409 appeared at the bottom layer between 12:30 and 15:30 with values of  $2.0 \times 10^{-3}$  and  $6.75 \times 10^{-5} \text{ s}^{-1}$ ,  
 410 respectively. The maximum values were usually larger than that at low-altitude areas due to the  
 411 stronger solar UV radiation on the TP (Su et al., 2008; Xing et al., 2021; Yang et al., 2021; Liu et al.,  
 412 2022), but being consistent with the values on the TP reported by Lin et al. (2008). Moreover, it should  
 413 be noted that the values of  $J(HONO)$  and  $J(O(^1D))$  all decreased with the increase of altitude, which  
 414 was significantly different with previous studies in low altitudes (Ryan et al., 2018; Xing et al., 2021;  
 415 Xu et al., 2021).





416

417 Figure 7. Averaged diurnal vertical profiles of the (a) photolysis rate  $J(HONO)$ , (b) photolysis rate  
 418  $J(O^1D)$ , (c) OH radical production rates from HONO photolysis, (d) OH radical production rates from  
 419  $O_3$  photolysis. (e) shows the averaged vertical profiles of OH radical production rates from HONO and  
 420  $O_3$  photolysis from 01 May to 09 July 2019.

421 Figure 7(c-d) showed the averaged diurnal vertical profiles of OH production rates from HONO and  $O_3$   
 422 photolysis from May to July 2019.  $P(OH)_{HONO}$  exhibited a multi-peak pattern which mainly appeared  
 423 before 10:00, 15:00-16:00, and after 19:00 at 0-0.4 km with a maximum value of 0.81 ppb/h. While  
 424  $P(OH)_{O_3}$  showed a unimodal pattern occurring at 13:00-15:00 under 0.4 km with a maximum value of  
 425 6.20 ppb/h. The averaged vertical profiles of  $P(OH)_{HONO}$  and  $P(OH)_{O_3}$  during the observation were  
 426 depicted in Figure 7(e). We found that the maximum values of  $P(OH)_{HONO}$  (0.49 ppb/h) and  $P(OH)_{O_3}$   
 427 (2.61 ppb/h) all appeared at the bottom layer, and decreased with height. That indicated  $O_3$  was an  
 428 important contributor of OH production ( $> 80\%$ ) on the TP, which was about 5-6 times to HONO.  
 429 Moreover, the OH production rates from HONO and  $O_3$  in other cities of China were depicted in Table  
 430 3. The contribution percentage of  $O_3$  to  $P(OH)$  in Nam Co was significantly higher than that in other  
 431 cities, which was due to the relatively high concentrations of  $O_3$  and  $H_2O$ , and the strong radiation in  
 432 Nam Co. In addition,  $P(OH)_{HONO}$  in Nam Co was close to that in relatively dry areas (i.e. Beijing and  
 433 Xianghe), but slightly lower than that in areas with relatively high humidity which can enhance the  
 434 heterogeneous production of HONO (Ryan et al., 2018; Liu et al., 2019; Xing et al., 2021).

435 Table 3. The maximum OH production rates contributed from HONO and  $O_3$  at different locations.

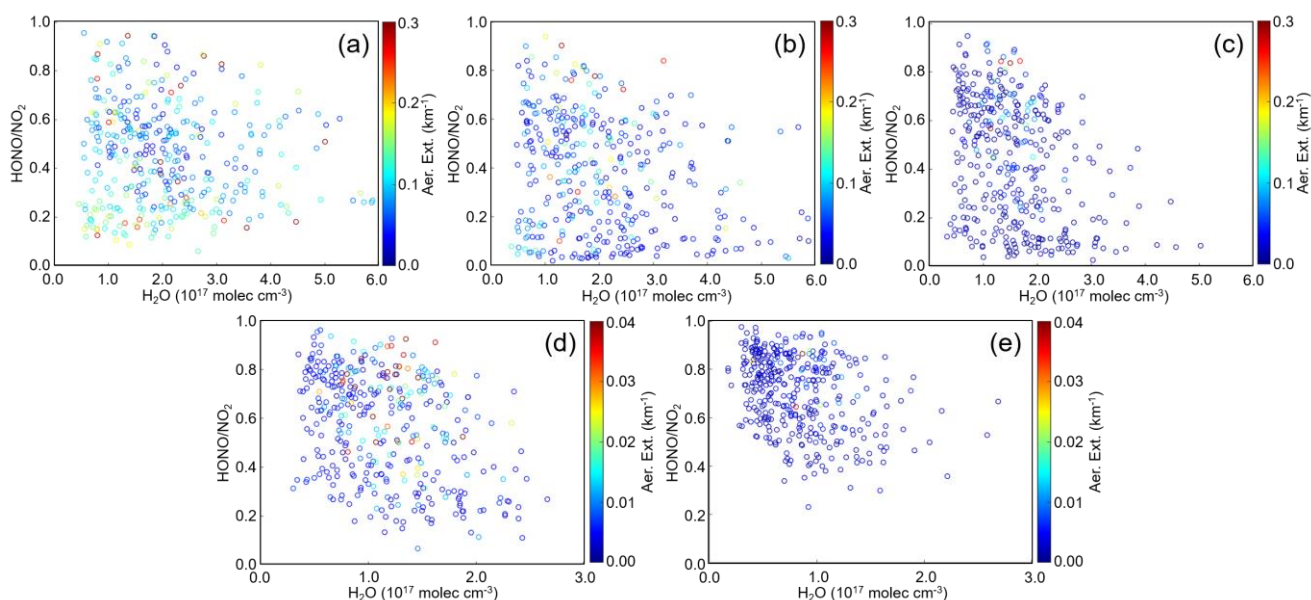
Location	Date	$P(OH)_{HONO}$ (ppb/h)	$P(OH)_{O_3}$ (ppb/h)	References
Xianghe (China)	Jul. 2008-Apr. 2009	~0.80 in Spring ~0.70 in Summer	~0.20 in Spring, ~0.45 in Summer	Hendrick et al. (2014)
Beijing (China)	Mar. 2010-Dec. 2012	~1.25 in Spring, ~0.70 in Summer	~0.10 in Spring, ~0.55 in Summer	Hendrick et al. (2014)
East China Sea (China)	Jun. 2017	~1.75	~1.20	Cui et al. (2019)
Chengdu (China)	Aug.-Sep. 2019	~3.25	-	Yang et al. (2021)
Qingdao (China)	Jul.-Aug. 2019	~1.30	~1.00	Yang et al. (2021)
Nam Co (China)	May-Jul. 2019	0.81	6.20	This study

436

#### 4.2 Possible daytime HONO sources

437 Atmospheric HONO mainly sourced from direct emission, homogeneous reaction and heterogeneous  
 438 reaction (Fu et al., 2019; Ren et al., 2020; Chai et al., 2021; Crilley et al., 2021; Li et al., 2021). There  
 439 were less anthropogenic emissions for HONO around NAMORS, however, the open burning of crop  
 440 residues and soil emissions should be important HONO sources considering the pasture environment  
 441 and large amounts of animal manure (Cui et al., 2021a; 2021b). Moreover, the background of low-level  
 442 NO on the TP led to the homogeneous reaction not to be the main source of HONO at NAMORS  
 443 (Lin et al., 2019; Xing et al., 2021; Li et al., 2022). Heterogeneous reaction of  $NO_2$  on wet surfaces  
 444 became an important potential source of HONO around NAMORS, which affected by the humidity,

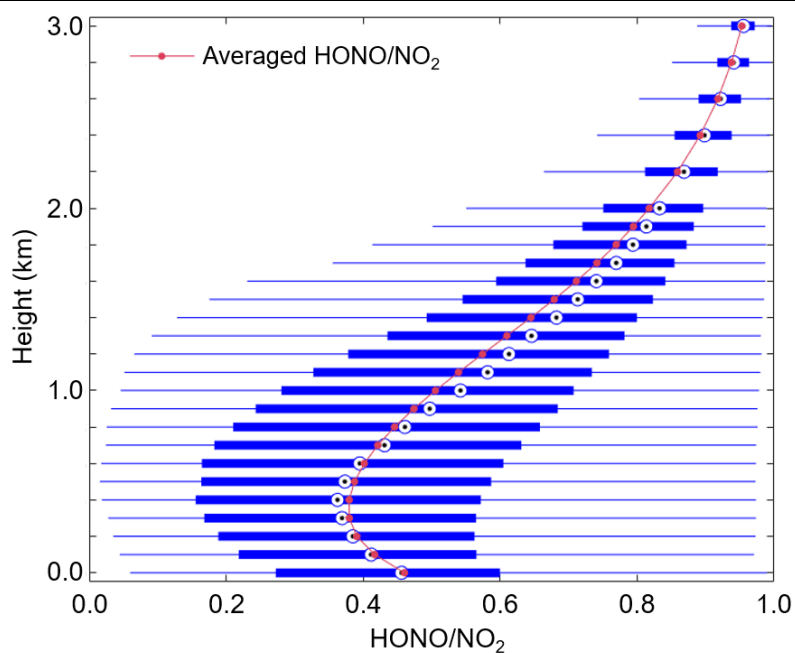
445 temperature, solar radiation, aerosol concentration and corresponding specific surface area. In order to  
 446 remove the effect of diurnal PBL evolution, we used HONO/NO<sub>2</sub> to indicate the extent of the  
 447 heterogeneous reaction process. As shown in Figure 8, scatter plots between HONO/NO<sub>2</sub> and H<sub>2</sub>O  
 448 were illustrated. We found that the maximum value of HONO/NO<sub>2</sub> appeared around water vapor being  
 449 around  $1.0 \times 10^{17}$  molec cm<sup>-3</sup> under 1.0 km, and being around  $0.5\text{-}1.0 \times 10^{17}$  molec cm<sup>-3</sup> at 1.0-2.0 km  
 450 height layer. This phenomenon of HONO/NO<sub>2</sub> firstly increasing and then decreasing with the  
 451 increasing of H<sub>2</sub>O (or relative humidity) was usually found in low-altitude areas in previous studies  
 452 (Wang et al., 2013; Liu et al., 2019; Xing et al., 2021; Xu et al., 2021). When the H<sub>2</sub>O was greater than  
 453 above mentioned critical values at different heights, HONO/NO<sub>2</sub> gradually decreased, which was  
 454 related to the efficient uptake of HONO and the decrease of NO<sub>2</sub> reactivity with the increase of H<sub>2</sub>O  
 455 (Liu et al., 2019; Xu et al., 2021). That indicated H<sub>2</sub>O has significant enhancement for the conversion  
 456 rate of NO<sub>2</sub> to HONO. Moreover, we found that the high value areas of HONO/NO<sub>2</sub> at above five  
 457 height layers were all accompanied by high aerosol extinction ( $> 0.15$  km<sup>-1</sup> under 1.0 km, and  $> 0.02$   
 458 km<sup>-1</sup> at 1.0-2.0 km). It indicated that aerosol surface has contribution to the heterogeneous reaction  
 459 process of NO<sub>2</sub>. The scatter plots between HONO and NO<sub>2</sub> at above five layers (Figure S11) also  
 460 confirmed the possibility of the NO<sub>2</sub> heterogeneous reaction to generate HONO on the TP, and the  
 461 contribution of atmospheric H<sub>2</sub>O and aerosol extinction to this process.



462  
 463 Figure 8. Scatter plots between HONO/NO<sub>2</sub> and H<sub>2</sub>O colored by aerosol extinction at (a) 0.0-0.2 km, (b)  
 464 0.4-0.6 km, (c) 0.8-1.0 km, (d) 1.2-1.4 km, and (e) 1.6-1.8 km from 1<sup>st</sup> May to 9<sup>th</sup> July 2019.

465 In Figure 9, the vertical profile of HONO/NO<sub>2</sub> from May to July 2019 was depicted. We found that  
 466 HONO/NO<sub>2</sub> firstly decreased and then increased with the increasing of height, which was opposite to  
 467 previous studies in low-altitude areas (Meng et al., 2020; Zhang et al., 2020; Xing et al., 2021; Xu et al.,  
 468 2021). The minimum average HONO/NO<sub>2</sub> occurred at 0.3-0.4 km height layer with a value of 0.37.  
 469 The relatively high values of HONO/NO<sub>2</sub> at the bottom layer should be related to the non-deducted  
 470 HONO direct emissions.





471

472 Figure 9. Statistics for the vertical profile of HONO/NO<sub>2</sub> from 1<sup>st</sup> May to 9<sup>th</sup> July 2019. The left and  
 473 right of the blue box represent the 25<sup>th</sup> and 75<sup>th</sup> percentiles, respectively; the dot within the box  
 474 represents the mean.

475 **4.3 Possible daytime O<sub>3</sub> sources**

476 In addition to local photochemistry process, long-range transport was the main source of O<sub>3</sub> on the TP  
 477 (Yin et al., 2017; Xu et al., 2018). To further understand the transport pathway and potential source of  
 478 O<sub>3</sub>, cluster analysis, WPSCF and WCWT models were used to assess the regional representivity of  
 479 O<sub>3</sub> at five typical heights (200 m, 600 m, 1000 m, 1400 m and 1800 m). As shown in Figure S12 and  
 480 Table 4, the backward trajectories arriving at NAMORS during the observation were classified into  
 481 three clusters at 200 m, 600 m, 1400 m, 1800 m, and four clusters at 1000 m. We found that cluster 3  
 482 was associated with the highest O<sub>3</sub> concentration at 200 m ( $65.48 \pm 17.41$  ppb) and 1800 m ( $49.69 \pm$   
 483  $2.21$  ppb), and cluster 1 were related to the highest O<sub>3</sub> concentration at 600 m ( $54.67 \pm 6.94$  ppb), 1000  
 484 m ( $51.61 \pm 3.84$  ppb) and 1400 m ( $50.51 \pm 2.89$  ppb). These two clusters were all originating from  
 485 northwestern of south Asian subcontinent passing through Himalayas, which was also reported by Yin  
 486 et al. (2017) during springtime from 2011 to 2015. In Figure S13 and 10, WPSCF and WCWT analysis  
 487 told us that the high O<sub>3</sub> concentration at above heights potentially sourced from northern India, central  
 488 Pakistan, Nepal, western Bhutan and northern Bangladesh through long-range transport. It should be  
 489 noted that the potential contribution to O<sub>3</sub> at NAMORS at 200 m from above potential source areas  
 490 were all over 40 ppb. These contributions from the mentioned potential source areas at other four  
 491 heights were also over 20-30 ppb. The massive fire emissions during springtime were an important  
 492 source of O<sub>3</sub> in south Asia (Jena et al., 2015), and the obvious burning during the observation was  
 493 observed in Figure S14. Moreover, the abundant precursors and high photochemical activity were  
 494 another significant sources of O<sub>3</sub> in south Asia (Kumar et al., 2012; Sharma et al., 2017).

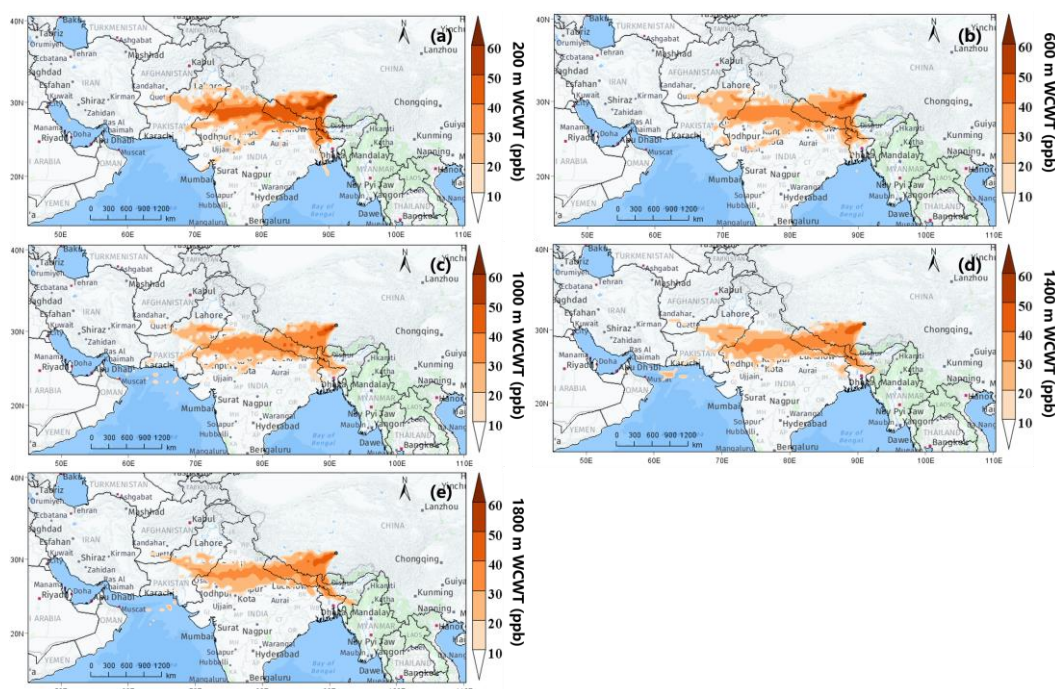
495 In addition, Figure 10 showed that the contribution of O<sub>3</sub> transported from Himalayas can even up to  
 496 50 ppb, especially under 600 m. Several previous studies have revealed that the stratospheric O<sub>3</sub>  
 497 intrusion events were frequent in the Himalayas during spring and summer (Cristofanelli et al., 2010;  
 498 Chen et al., 2011; Škerlak et al., 2014; Putero et al., 2016). Therefore, the O<sub>3</sub> from stratospheric  
 499 intrusions in the Himalayas can affect the O<sub>3</sub> at NAMORS through long-range transport.

500 Table 4. Trajectory ratios and averaged O<sub>3</sub> concentration for all trajectory clusters arriving in Nam Co  
 501 at 200 m, 600 m, 1000 m, 1400 m and 1800 m from May to July 2019.

	Cluster	Traj_ratio	O <sub>3</sub> concentration (ppb)
			Mean $\pm$ SD

200 m	1	55.86%	$61.50 \pm 18.15$
	2	11.85%	$54.57 \pm 14.67$
	3	32.28%	$65.48 \pm 17.41$
	All	100.00%	$61.14 \pm 17.74$
600 m	1	62.55%	$54.67 \pm 6.94$
	2	14.32%	$50.43 \pm 6.64$
	3	23.13%	$53.27 \pm 7.63$
	All	100.00%	$53.39 \pm 7.26$
1000 m	1	49.16%	$51.61 \pm 3.84$
	2	8.81%	$49.60 \pm 3.99$
	3	22.73%	$50.72 \pm 4.21$
	4	19.30%	$51.39 \pm 4.49$
	All	100.00%	$50.98 \pm 4.30$
1400 m	1	80.14%	$50.51 \pm 2.89$
	2	4.95%	$49.12 \pm 2.73$
	3	14.92%	$49.44 \pm 3.85$
	All	100.00%	$50.07 \pm 3.15$
1800 m	1	83.75%	$49.68 \pm 2.55$
	2	0.00%	$49.07 \pm 2.23$
	3	16.25%	$49.69 \pm 2.21$
	All	100.00%	$49.59 \pm 2.49$

502



503

504 Figure 10. Spatial distributions of WCWT values for O<sub>3</sub> at (a) 200 m, (b) 600 m, (c) 1000 m, (d) 1400  
505 m, and (e) 1800 m height layers from 01<sup>st</sup> May to 09<sup>th</sup> July 2019 over CAS (NAMORS).

## 506 5 Summary and conclusions

507 MAX-DOAS measurements were performed to clarify the vertical distributions of several atmospheric  
508 components (aerosol, H<sub>2</sub>O, NO<sub>2</sub>, HONO and O<sub>3</sub>), and to explore the AOC in vertical space in Nam Co  
509 from May to July 2019. The MAX-DOAS NO<sub>2</sub>, HONO and O<sub>3</sub> agreed well with in situ measurements,  
510 with correlation coefficients of 0.91, 0.62 and 0.82, respectively. We found that the averaged vertical

511 profiles of aerosol, H<sub>2</sub>O, HONO and O<sub>3</sub> all exhibited an exponential shape, while NO<sub>2</sub> showed a  
512 Gaussian shape with a maximum value of 0.32 ppb appearing at 300-400 m. The maximum  
513 concentrations of monthly averaged aerosol (0.17 km<sup>-1</sup>) and O<sub>3</sub> (66.71 ppb) appeared on May, H<sub>2</sub>O  
514 ( $3.68 \times 10^{17}$  molec cm<sup>-3</sup>) and HONO (0.13 ppb) appeared on July, and NO<sub>2</sub> (0.39 ppb) occurred on  
515 June. For the diurnal variation, above five species all mainly distributed under 1.0 km, and mostly  
516 exhibited a multi-peak pattern considering the effect of regional transport and local chemical reaction.

517 O<sub>3</sub> and HONO were important source of OH on the TP. The diurnal averaged OH production rate from  
518 HONO during the observation exhibited a multi-peak pattern appearing before 10:00, 15:00-16:00 and  
519 after 19:00 under 0.4 km with the maximum value of 0.81 ppb/h. The OH production rate from O<sub>3</sub>  
520 shown a unimodal pattern occurring at 13:00-15:00 under 0.4 km with the maximum value of 6.20  
521 ppb/h which was obviously higher than that at low-altitude areas. In addition to direct emission, the  
522 heterogeneous reaction of NO<sub>2</sub> on wet surfaces was also an important source of HONO in Nam Co. We  
523 found that HONO/NO<sub>2</sub> first increasing and then decreasing with the increasing of H<sub>2</sub>O. The maximum  
524 value of HONO/NO<sub>2</sub> appeared around H<sub>2</sub>O being around  $1.0 \times 10^{17}$  molec cm<sup>-3</sup> under 1.0 km, and  
525 being around  $1.0\text{-}2.0 \times 10^{17}$  molec cm<sup>-3</sup> at 1.0-2.0 km height layer. Moreover, high values of  
526 HONO/NO<sub>2</sub> usually accompanied by high aerosol extinction. O<sub>3</sub> under 2.0 km were potentially sourced  
527 from Himalayas, northern India, central Pakistan, Nepal, western Bhutan and northern Bangladesh  
528 through long-range transport. Our results draw a picture of further understanding the spatial and  
529 temporal variations in oxidation chemistry under PBL and provided a new perspective for source  
530 analysis of major atmospheric components through vertical observation on the TP.

### 531 **Data availability**

532 All measurement data used in this study can be made available for scientific purposes upon request to  
533 the authors (chliu81@ustc.edu.cn & xingcz@aiofm.ac.cn).

### 534 **Author contribution**

535 CX, CL, and CY designed the research and organization this paper. CX wrote this paper, and CL and  
536 CY edited it. CX, JX, HW, XJ contributed to the retrieval of MAX-DOAS vertical profile data and  
537 satellite data. CX, CL, CY, JO, and QH contributed to data analysis. All the above authors contributed  
538 to the revision of the manuscript.

### 539 **Acknowledgements**

540 We firstly would like to thank @Tibet group for effectively organizing the Nam Co observation. We  
541 also would like to thank Peking University (Chunxiang Ye's group) and Anhui Institute of Optics and  
542 Fine Mechanics (Weixiong Zhao's group) to provide the DOAS validation data of HONO, O<sub>3</sub> and NO<sub>2</sub>.  
543 We thank the National Oceanic and Atmospheric Administration (NOAA) Air Resources Laboratory  
544 (ARL) for providing the open HYSPLIT transport and dispersion model. This study was supported by  
545 the National Natural Science Foundation of China (42225504 and U21A2027), the Anhui Provincial  
546 Natural Science Foundation (2108085QD180), and the Presidential Foundation of the Hefei Institutes  
547 of Physical Science, Chinese Academy Sciences (YZJJ2021QN06).

### 548 **Competing interests**

549 All authors declare that they have no conflict of interest or financial conflicts to disclose.

550

### 551 **References**

- 552 [1] Kang, S., Chen, P., Li, C., Liu, B., and Cong, Z.: Atmospheric Aerosol Elements over the Inland Tibetan Plateau:  
553 Concentration, Seasonality, and Transport, *Aerosol Air Qual. Res.*, 16: 789–800, doi: 10.4209/aaqr.2015.05.0307,  
554 2016.  
555 [2] Xia, X., Zong, X., Cong, Z., Chen, H., Kang, S., and Wang, P.: Baseline continental aerosol over the central  
556 Tibetan plateau and a case study of aerosol transport from South Asia, *Atmos. Environ.*, 45, 7370-7378, doi:  
557 10.1016/j.atmosenv.2011.07.067, 2011.

- 558 [3] Xing, C., Liu, C., Wang, S., Hu, Q., Liu, H., Tan, W., Zhang, W., Li, B., and Liu, J.: A new method to determine  
559 the aerosol optical properties from multiple-wavelength O<sub>4</sub> absorption by MAX-DOAS observation, *Atmos. Meas.*  
560 *Tech.*, 12, 3289-3302, doi.org/10.5194/amt-12-3289-2019, 2019.
- 561 [4] Zhao, F., Liu, C., Cai, Z., Liu, X., Bak, J., Kim, J., Hu, Q., Xia, C., Zhang, C., Sun, Y., Wang, W., and Liu, J.:  
562 Ozone profile retrievals from TROPOMI: Implication for the variation of tropospheric ozone during the outbreak of  
563 COVID-19 in China, *Sci. Total Environ.*, 764, 142886, doi.org/10.1016/j.scitotenv.2020.142886, 2021.
- 564 [5] Fang, B., Zhao, W., Xu, X., Zhou, J., Ma, X., Wang, S., Zhang, W., Venables, D.S., and Chen, W.: Portable  
565 broadband cavity-enhanced spectrometer utilizing Kalman filtering: application to real-time, in situ monitoring of  
566 glyoxal and nitrogen dioxide, *Opt. Express*, 25(22), 26910-26922, doi.org/10.1364/OE.25.026910, 2017.
- 567 [6] Kleffmann, J., Wiesen, P.: Technical Note: Quantification of interferences of wet chemical HONO LOPAP  
568 measurements under simulated polar conditions, *Atmos. Chem. Phys.*, 8, 6813-6822,  
569 doi.org/10.5194/acp-8-6813-2008, 2008.
- 570 [7] Bessho, K., Date, K., Hayashi, M., Ikeda, A., Imai, T., Inoue, H., Kumagai, Y., Miyakawa, T., Murata, H., Ohno,  
571 T., Okuyama, A., Oyama, R., Sasaki, Y., Shimazu, Y., Shimoji, K., Sumida, Y., Suzuki, M., Taniguchi, H.,  
572 Tsuchiyama, H., Uesawa, D., Yokota, H., and Yoshida, R.: An Introduction to Himawari-8/9-Japan's New-Generation  
573 Geostationary Meteorological Satellites, *J. Meteorol. Soc. Jan.*, 94(2), 151-183, doi: 10.2151/jmsj.2016-009, 2016.
- 574 [8] Veefkind, J.P., de Haan, J.F., Brinksma, E.J., Kroon, M., and Levelt, P.F.: Total Ozone From the Ozone  
575 Monitoring Instrument (OMI) Using the DOAS Technique, *IEEE T. Geosci. Remote Sens.*, 44(5), 1239-1244, doi:  
576 10.1109/TGRS.2006.871204, 2004.
- 577 [9] Griffin, D., Zhao, X., Mclinden, C.A., Boersma, F., Bourassa, A., Dammers, E., Degenstein, D., Eskes, H., Fehr,  
578 L., Fioletov, V., Hayden, K., Kharol, S.K., Li, S., Makar, P., Martin, R.V., Mihele, C., Mittermeier, R.L., Krotkov, N.,  
579 Sneep, M., Lamsal, L.N., ter Linden, M., van Geffen, J., Veefkind, P., and Wolde, M.: High-Resolution Mapping of  
580 Nitrogen Dioxide With TROPOMI: First Results and Validation Over the Canadian Oil Sands, *Geophys. Res. Lett.*,  
581 46, 1049-1060, doi: 10.1029/2018GL081095, 2018.
- 582 [10] Su, W., Liu, C., Chan, K.L., Hu, Q., Liu, H., Ji, X., Zhu, Y., Liu, T., Zhang, C., Chen, Y., and Liu, J.: An  
583 improved TROPOMI tropospheric HCHO retrieval over China, *Atmos. Meas. Tech.*, 13, 6271-6292,  
584 doi.org/10.5194/amt-13-6271-2020, 2020.
- 585 [11] Grell, G.A., Peckham, S.E., Schmitz, R., McKeen, S.A., Frost, G., Skamarock, W.C., and Eder, B.: Fully coupled  
586 "online" chemistry with the WRF model, *Atmos. Environ.*, 39(37), 6957-6975,  
587 doi.org/10.1016/j.atmosenv.2005.04.027, 2005.
- 588 [12] Shi, G., Yang, L., Wang, Y., Kobayashi, K., Zhu, J., Tang, H., Pan, S., Chen, T., Liu, G., and Wang, Y.: Impact  
589 of elevated ozone concentration on yield of four Chinese rice cultivars under fully open-air field conditions, *Agr.*  
590 *Ecosys. Environ.*, 131(3-4), 178-184, doi.org/10.1016/j.agee.2009.01.009, 2009.
- 591 [13] Yin, X., Kang, S., de Foy, B., Cong, Z., Luo, J., Zhang, L., Ma, Y., Zhang, G., Rupakheti, D., and Zhang, Q.:  
592 Surface ozone at Nam Co in the inland Tibetan Plateau: variation, synthesis comparison and regional  
593 representativeness, *Atmos. Chem. Phys.*, 17, 11293-11311, doi.org/10.5194/acp-17-11293-2017, 2017.
- 594 [14] Draxler, R.R., Hess, G.: An overview of the HYSPLIT\_4 modelling system for trajectories, *Aust. Meteorol. Mag.*,  
595 47, 295-308, 1998.
- 596 [15] Hong, Q., Liu, C., Hu, Q., Xing, C., Tan, W., Liu, H., Huang, Y., Zhu, Y., Zhang, J., Geng, T., and Liu, J.:  
597 Evolution of the vertical structure of air pollutants during winter heavy pollution episodes: The role of regional  
598 transport and potential sources, *Atmos. Res.*, 228, 106-222, doi.org/10.1016/j.atmosres.2019.05.016, 2019.
- 599 [16] Ou, J., Hu, Q., Liu, H., Hong, Q., Xing, C., Tan, W., Lin, H., Wang, X., Xu, H., Zhu, P., and Liu, W.: Vertical  
600 characterization and potential sources of aerosols in different seasons over the Yangtze River Delta using  
601 ground-based MAX-DOAS, *Environ. Pollut.*, 279, 116898, doi.org/10.1016/j.envpol.2021.116898, 2021.
- 602 [17] Hsu, Y.K., Holsen, T.M., Hopke, P.K.: Comparison of hybrid receptor models to locate PCB sources in Chicago,  
603 *Atmos. Environ.*, 37, 545-562, doi.org/10.1016/S1352-2310(02)00886-5, 2003.
- 604 [18] Wang, Y., Zhang, X., Draxler, R.R.: TrajStat: GIS-based software that uses various trajectory statistical analysis  
605 methods to identify potential sources from long-term air pollution measurement data, *Environ. Model Softw.*, 24,  
606 938-939, doi.org/10.1016/j.envsoft.2009.01.004, 2009.
- 607 [19] Ye, C.: The first constraint of atmospheric oxidative capacity in Namco, a background Tibetan Plateau research  
608 site, *AGU Fall Meeting Abstracts*, 2019:A51C-08, 2019.
- 609 [20] Lin, W., Zhu, T., Song, Y., Zou, H., Tang, M., Tang, X., and Hu, J.: Photolysis of surface O<sub>3</sub> and production  
610 potential of OH radicals in the atmosphere over the Tibetan Plateau, *J. Geophys. Res.-Atmos.*, 113, D02309,  
611 doi:10.1029/2007JD008831, 2008.
- 612 [21] Michoud, V., Kukui, A., Camredon, M., Colomb, A., Borbon, A., Miet, K., Aumont, B., Beekmann, M.,  
613 Durand-Jolibois, R., Perrier, S., Zapf, P., Siour, G., Ait-Helal, W., Locoge, N., Sauvage, S., Afif, C., Gros, C., Furger,  
614 M., Ancellet, G., and Doussin, J.F.: Radical budget analysis in a suburban European site during the MEGAPOLI  
615 summer field campaign, *Atmos. Chem. Phys.*, 12, 11951-11974, doi.org/10.5194/acp-12-11951-2012, 2012.
- 616 [22] Ryan, R.G., Rhodes, S., Tully, M., Wilson, S., Jones, N., Frieß, U., and Schofield, R.: Daytime HONO, NO<sub>2</sub> and  
617 aerosol distributions from MAX-DOAS observations in Melbourne, *Atmos. Chem. Phys.*, 18, 13969-13958,  
618 doi.org/10.5194/acp-18-13969-2018, 2018.

- 619 [23] Xue, C., Zhang, C., Ye, C., Liu, P., Catoire, V., Krysztofiak, G., Chen, H., Ren, Y., Zhao, X., Wang, J., Zhang, F.,  
620 Zhang, C., Zhang, J., An, J., Wang, T., Chen, J., Kleffmann, J., Mellouki, A., and Mu, Y.: HONO budget and its role  
621 in nitrate formation in rural North China Plain, *Environ. Sci. Tech.*, 54, 18, 11048-11057,  
622 doi.org/10.1021/acs.est.0c01832, 2020.
- 623 [24] Xing, C., Liu, C., Wu, H., Lin, J., Wang, F., Wang, S., and Gao, M.: Ground-based vertical profile observations  
624 of atmospheric composition on the Tibetan Plateau (2017-2019), *Earth Syst. Sci. Data*, 13, 4897-4912,  
625 doi.org/10.5194/essd-13-4897-2021, 2021a.
- 626 [25] Xing, C., Liu, C., Hu, Q., Fu, Q., Wang, S., Lin, H., Zhu, Y., Wang, S., Wang, W., Javed, Z., Ji, X., Liu, J.:  
627 Vertical distributions of wintertime atmospheric nitrogenous compounds and the corresponding OH radicals  
628 production in Leshan, southwest China, *J. Environ. Sci.*, 105, 44-55, doi.org/10.1016/j.jes.2020.11.019.
- 629 [26] Luo, S., Holland, F., Rohrer, F., Lu, K., Bohn, B., Brauers, T., Chang, C.C., Fuchs, H., Häsel, R., Kita, K.,  
630 Kondo, Y., Li, X., Shao, M., Zeng, L., Wahner, A., Zhang, Y., Wang, W., Hofzumahaus, A.: Atmospheric OH  
631 reactivities in the Pearl River Delta-China in summer 2006: measurement and model results, *Atmos. Chem. Phys.*, 10,  
632 11243-11260, doi.org/10.5194/acp-10-11243-2010, 2010.
- 633 [27] Yang, Y., Wang, Y., Huang, W., Yao, D., Zhao, S., Wang, Y., Ji, D., Zhang, R., Wang, Y.: Parameterized  
634 atmospheric oxidation capacity and speciated OH reactivity over a suburban site in the North China Plain: A  
635 comparative study between summer and winter, *Sci. Total Environ.*, 773, 145264,  
636 doi.org/10.1016/j.scitotenv.2021.145264, 2021.
- 637 [28] Ma, Y., Zhong, L., Su, Z.: Energy and water cycles in the third pole, *Water*, 14(7), 1175,  
638 doi.org/10.3390/w14071175, 2022.
- 639 [29] Kang, S., Zhang, Y., Chen, P., Guo, J., Zhang, Q., Cong, Z., Kaspari, S., Tripathee, L., Gao, T., Niu, H., Zhong,  
640 X., Chen, X., Hu, Z., Li, X., Li, Y., Neupane, B., Yan, F., Rupakheti, D., Gul, C., Zhang, W., Wu, G., Yang, L., Wang,  
641 Z., Li, C.: Black carbon and organic carbon dataset over the Third Pole, *Earth Syst. Sci. Data*, 14, 683-707,  
642 doi.org/10.5194/essd-14-683-2022, 2022.
- 643 [30] Ma, Y., Hu, Z., Xie, Z., Ma, W., Wang, B., Chen, X., Li, M., Zhong, L., Sun, F., Gu, L., Han, C., Zhang, L., Liu,  
644 X., Ding, Z., Sun, G., Wang, S., Wang, Y., and Wang, Z.: A long-term (2005-2016) dataset of integrated  
645 land-atmosphere interaction observations on the Tibetan Plateau, *Earth Syst. Sci. Data*, 12, 2937-2957,  
646 doi:10.5194/essd-12-2937-2020, 2020.
- 647 [31] Qu, B., Zhang, Y., Kang, S., Sillanpää, M.: Water quality in the Tibetan Plateau: Major ions and trace elements  
648 in rivers of the “Water Tower of Asia”, *Sci. Total Environ.*, 649, 571-581, doi.org/10.1016/j.scitotenv.2018.08.316,  
649 2019.
- 650 [32] Zhou, S., Sun, F., Wang, M., Zhou, S., and Qing, Y.: Effects of atmospheric heat source on the Tibetan Plateau  
651 vortex in different stages: A case study in June 2016, *Atmosphere*, 13(5), 689, doi.org/10.3390/atmos13050689, 2022.
- 652 [33] Liu, J., Guan, X., Gao, Z., Huang, X., Ma, J., He, Y., and Xie, T.: Inter-decadal variability of the heat source over  
653 the Tibetan Plateau, *Clim. Dynam.*, 58, 729-739, doi.org/10.1007/s00382-021-05929-z, 2022.
- 654 [34] Chen, P., Kang, S., Bai, J., Sillanpää, M., Li, C.: Yak dung combustion aerosols in the Tibetan Plateau: Chemical  
655 characteristics and influence on the local atmospheric environment, *Atmos. Res.*, 156, 58-66,  
656 doi.org/10.1016/j.atmosres.2015.01.001, 2015.
- 657 [35] Boos, W. R. and Kuang, Z.: Dominant control of the South Asian monsoon by orographic insulation versus  
658 plateau heating, *Nature*, 463, 218-222, doi:10.1038/nature08707, 2010.
- 659 [36] Yanai, M., Li, C., and Song, Z.: Seasonal Heating of the Tibetan Plateau and Its Effects on the Evolution of the  
660 Asian Summer Monsoon, *J. Meteorol. Soc. Jpn. Ser. II*, 70, 319-351, doi:10.2151/jmsj1965.70.1B\_319, 1992.
- 661 [37] Li, C., Zou, Q., Xu, X., and Gao, S.: Water vapor transport around the Tibetan Plateau and its effect on summer  
662 rainfall over the Yangtze River valley, *J. Meteorol. Res.*, 30, 472-482, doi: 10.1007/s13351-016-5123-1, 2016.
- 663 [38] Lei, Y., Zhu, Y., Wang, B., Yao, T., Yang, K., Zhang, X., Zhai, J., and Ma, N.: Extreme lake level changes in the  
664 Tibetan Plateau associated with the 2015/2016 El Niño, *Geophys. Res. Lett.*, 46, 11, 5889-5898,  
665 doi.org/10.1029/2019GL081946, 2019.
- 666 [39] Hsu, H-H., and Liu, X.: Relationship between the Tibetan Plateau heating and East Asian summer monsoon  
667 rainfall, *Geophys. Res. Lett.*, 30, 20, doi.org/10.1029/2003GL017909, 2003.
- 668 [40] Zhang, L., Guo, X., Zhao, T., Gong, S., Xu, X., Li, Y., Luo, L., Gui, K., Wang, H., Zheng, Y., and Yin, X.: A  
669 modelling study of the terrain effects on the haze pollution in Sichuan Basin, *Atmos. Environ.*, 196, 77-85,  
670 doi.org/10.1016/j.atmosenv.2018.10.007, 2019.
- 671 [41] Barnett, T. P., Adam, J. C., and Lettenmaier, D. P.: Potential impacts of a warming climate on water availability  
672 in snow-dominated regions, *Nature*, 438, 303-309, doi:10.1038/nature04141, 2005.
- 673 [42] Bolch, T., Kulkarni, A., Kaab, A., Huggel, C., Paul, F., Cogley, J. G., Frey, H., Kargel, J. S., Fujita, K., Scheel,  
674 M., Bajracharya, S., and Stoffel, M.: The State and Fate of Himalayan Glaciers, *Science*, 336, 310-314,  
675 doi:10.1126/science.1215828, 2012.
- 676 [43] Cong, Z., Kang, S., Kawamura, K., Liu, B., Wan, X., Wang, Z., Gao, S., and Fu, P.: Carbonaceous aerosols on  
677 the south edge of the Tibetan Plateau: concentrations, seasonality and sources, *Atmos. Chem. Phys.*, 15, 1573-1584,  
678 https://doi.org/10.5194/acp-15-1573-2015, 2015.

- 679 [44] Kang, S. C., Huang, J., Wang, F. Y., Zhang, Q. G., Zhang, Y. L., Li, C. L., Wang, L., Chen, P. F., Sharma, C. M.,  
680 Li, Q., Sillanpaa, M., Hou, J. Z., Xu, B. Q., and Guo, J. M.: Atmospheric Mercury Depositional Chronology  
681 Reconstructed from Lake Sediments and Ice Core in the Himalayas and Tibetan Plateau, *Environ. Sci. Technol.*, 50,  
682 2859–2869, doi:10.1021/acs.est.5b04172, 2016.
- 683 [45] Ran, L., Deng, Z., Wu, Y., Li, J., Bai, Z., Lu, Y., Zhuoga, D., and Bian J.: Measurement report: Vertical  
684 profiling of particle size distributions over Lhasa, Tibet – tethered balloon-based in situ measurements and source  
685 apportionment, *Atmos. Chem. Phys.*, 22, 6217–6229, doi.org/10.5194/acp-22-6217-2022, 2022.
- 686 [46] Wang, K., Hattori, S., Lin, M., Ishino, S., Alexander, B., Kamezaki, K., Yoshida, N., and Kang, S.: Isotopic  
687 constraints on atmospheric sulfate formation pathways in the Mt. Everest region, southern Tibetan Plateau, *Atmos.*  
688 *Chem. Phys.*, 21, 8357–8376, https://doi.org/10.5194/acp-21-8357-2021, 2021.
- 689 [47] Che, J. and Zhao, P.: Characteristics of the summer atmospheric boundary layer height over the Tibetan Plateau  
690 and influential factors, *Atmos. Chem. Phys.*, 21, 5253–5268, https://doi.org/10.5194/acp-21-5253-2021, 2021.
- 691 [48] Sun, Y., Yin, H., Cheng, Y., Zhang, Q., Zheng, B., Notholt, J., Lu, X., Liu, C., Tian, Y., Liu, J.: Quantifying  
692 variability, source, and transport of CO in the urban areas over the Himalayas and Tibetan Plateau, *Atmos. Chem.*  
693 *Phys.*, 21, 9201–9222, https://doi.org/10.5194/acp-21-9201-2021, 2021.
- 694 [49] Li, R., Zhao, Y., Zhou, W., Meng, Y., Zhang, Z., and Fu, H.: Developing a novel hybrid model for the estimation  
695 of surface 8-h ozone (O<sub>3</sub>) across the remote Tibetan Plateau during 2005–2018, *Atmos. Chem. Phys.*, 20, 6159–6175,  
696 https://doi.org/10.5194/acp-20-6159-2020.
- 697 [50] Gao, M., Gao, J., Zhu, B., Kumar, R., Lu, X., Song, S., Zhang, Y., Jia, B., Wang, P., Beig, G., Hu, J., Ying, Q.,  
698 Zhang, H., Sherman, P., and McElroy, M. B.: Ozone pollution over China and India: seasonality and sources, *Atmos.*  
699 *Chem. Phys.*, 20, 4399–4414, https://doi.org/10.5194/acp-20-4399-2020, 2020.
- 700 [51] Rawat, P., and Naja, M.: Remote sensing study of ozone, NO<sub>2</sub>, and CO: some contrary effects of SARS-CoV-2  
701 lockdown over India, *Environ. Sci. Pollut. Res.*, 29, 22515–22530, doi:10.1007/s11356-021-17441-2, 2022.
- 702 [52] Huang, J., Minnis, P., Yi, Y., Tang, Q., Wang, X., Hu, Y., Liu, Z., Ayers, K., Trepte, C., and Winker, D.:  
703 Summer dust aerosols detected from CALIPSO over the Tibetan Plateau, *Geophys. Res. Lett.*, 34, L18805,  
704 https://doi.org/10.1029/2007GL029938, 2007.
- 705 [53] Li, R., Zhao, Y., Zhou, W., Meng, Y., Zhang, Z., and Fu, H.: Developing a novel hybrid model for the estimation  
706 of surface 8 h ozone (O<sub>3</sub>) across the remote Tibetan Plateau during 2005–2018, *Atmos. Chem. Phys.*, 20, 6159–6175,  
707 https://doi.org/10.5194/acp-20-6159-2020, 2020.
- 708 [54] Zhu, J., Xia, X., Che, H., Wang, J., Cong, Z., Zhao, T., Kang, S., Zhang, X., Yu, X., and Zhang, Y.:  
709 Spatiotemporal variation of aerosol and potential long-range transport impact over the Tibetan Plateau, China, *Atmos.*  
710 *Chem. Phys.*, 19, 14637–14656, https://doi.org/10.5194/acp-19-14637-2019, 2019.
- 711 [55] Xu, X., Sun, C., Chen, D., Zhao, T., Xu, J., Zhang, S., Li, J., Chen, B., Zhao, Y., Xu, H., Dong, L., Sun, X., and  
712 Zhu, Y.: A vertical transport window of water vapor in the troposphere over the Tibetan Plateau with implications for  
713 global climate change, *Atmos. Chem. Phys.*, 22, 1149–1157, https://doi.org/10.5194/acp-22-1149-2022, 2022.
- 714 [56] Xu, X., Wu, H., Yang, X., and Xie, L.: Distribution and transport characteristics of dust aerosol over Tibetan  
715 Plateau and Taklimakan Desert in China using MERRA-2 and CALIPSO data, *Atmos. Environ.*, 237, 117670,  
716 https://doi.org/10.1016/j.atmosenv.2020.117670, 2020.
- 717 [57] Yang, K., Koike, T., and Yang, D.: Surface flux parameterization in the Tibetan Plateau, *Bound.-Lay. Meteorol.*,  
718 106, 245–262, doi:10.1023/A:1021152407334, 2003.
- 719 [58] Seidel, D. J., Ao, C. O., and Li, K.: Estimating climatological planetary boundary layer heights from radiosonde  
720 observations: Comparison of methods and uncertainty analysis, *J. Geophys. Res.*, 115, D16113,  
721 https://doi.org/10.1029/2009JD013680, 2010.
- 722 [59] Dong, Q., Huang, Z., Li, W., Li, Z., Song, X., Liu, W., Wang, T., Bi, J., and Shi, J.: Polarization lidar  
723 measurements of dust optical properties at the junction of the Taklimakan Desert-Tibetan Plateau, *Remote Sens.*,  
724 14(3), 558, https://doi.org/10.3390/rs14030558, 2022.
- 725 [60] Zhang, J., Xia, X., and Wu, X.: First in situ UV profile across the UTLS accompanied by ozone measurement  
726 over the Tibetan Plateau, *J. Environ., Sci.*, 98, 71–76, doi:10.1016/j.jes.2020.05.020, 2020.
- 727 [61] Fang, X., Li, T., Ban, C., Wu, Z., Li, J., Li, F., Cen, Y., and Tian, B.: A mobile differential absorption lidar for  
728 simultaneous observations of tropospheric and stratospheric ozone over Tibet, *Opt. Express*, 27, 4126–4139,  
729 doi:10.1364/OE.27.004126, 2019.
- 730 [62] Wang, Y., Pukite, J., Wagner, T., Donner, S.; Beirle, S., Hilboll, A., Vrekoussis, M., Richter, A., Apituley, A.,  
731 Pipers, A., Allaart, M., Eskes, H., Frumau, A., van Roozendaal, M., Lampel, J., Platt, U., Schmitt, S., Swart, D., and  
732 Vonk, J.: Vertical profiles of tropospheric ozone from MAX-DOAS measurement during the CINDI-2 campaign: part  
733 1—Development of a new retrieval algorithm. *J. Geophys. Res. Atmos.* 123 (18), 10–637.  
734 https://doi.org/10.1029/2018JD028647, 2018.
- 735 [63] Xing, C., Liu, C., Wang, S., Chan, K.L., Gao, Y., Huang, X., Su, W., Zhang, C., Dong, Y., Fan, G., Zhang, T.,  
736 Chen, Z., Hu, Q., Su, H., Xie, Z., and Liu, J.: Observations of the vertical distributions of summertime atmospheric  
737 pollutants and the corresponding ozone production in Shanghai, China. *Atmos. Chem. Phys.* 17, 14275–14289.  
738 https://doi.org/10.5194/acp-17-14275-2017, 2017.



739 [64] Xing, C., Liu, C., Wang, S., Hu, Q., Liu, H., Tan, W., Zhang, W., Li, B., and Liu, J.: A new method to determine  
740 the aerosol optical properties from multiple-wavelength O<sub>4</sub> absorptions by MAX-DOAS observation. *Atmos. Meas.*  
741 *Tech.* 12, 3289–3302. <https://doi.org/10.5194/amt-12-3289-2019>, 2019.

742 [65] Xing, C., Liu, C., Hu, Q., Fu, Q., Lin, H., Wang, S., Su, W., Wang, W., Javed, Z., and Liu, J.: Identifying the  
743 wintertime sources of volatile organic compounds (VOCs) from MAX-DOAS measured formaldehyde and glyoxal in  
744 Chongqing, Southwest China. *Sci. Total Environ.* 715, 136258 <https://doi.org/10.1016/j.scitotenv.2019.136258>, 2020.

745 [66] Ye, D. Z., and Gao, Y. X.: *The Meteorology of the Tibetan Plateau* (in Chinese), 278pp., Science Press, Beijing,  
746 pp. 39–48, 1979.

747 [67] Liu, Y., and Li, W.: Deepening of the ozone valley over Tibetan Plateau and its possible influences (Chinese with  
748 English abstract), *Acta Meteorologica Sinica*, 59(1), 97–106, 2001.

749 [68] Yang, J., Kang, S., Hu, Y., Chen, X., Rai, M.: Influence of South Asian biomass burning on ozone and aerosol  
750 concentrations over the Tibetan Plateau, *Adv. Atmos. Sci.*, 39, 1184–1197, doi:10.1007/s00376-022-1197-0, 2022.

751 [69] Yu, J., Meng, L., Chen, Y., Zhang, H., and Liu, J.: Ozone profiles, precursors, and vertical distribution in urban  
752 Lhasa, Tibetan Plateau, *Remote Sens.*, 14(11), 2533, <https://doi.org/10.3390/rs14112533>, 2022.

753 [70] Li, M., Mao, J., Chen, S., Bian, J., Bai, Z., Wang, X., Chen, W., and Yu, P.: Significant contribution of lightning  
754 NO<sub>x</sub> to summertime surface O<sub>3</sub> on the Tibetan Plateau, *Sci. Total Environ.*, 829, 154639,  
755 doi:10.1016/j.scitotenv.2022.154639, 2022.

756 [71] Zhou, L., Zhang, X., Zhang, J.: Temporal and spatial distributions of atmospheric hydroxyl radicals based on the  
757 observation with the aura microwave limb sounder. *Science & Technology Review*, 33(17): 69–77, 2015.

758 [72] Yin, X., Kang, S., de Foy, B., Cong, Z., Luo, J., Zhang, L., Ma, Y., Zhang, G., Rupakheti, D., and Zhang, Q.:  
759 Surface ozone at Nam Co in the inland Tibetan Plateau: variation, synthesis comparison and regional  
760 representativeness, *Atmos. Chem. Phys.*, 17, 11293–11311, <https://doi.org/10.5194/acp-17-11293-2017>, 2017.

761 [73] Xu, X., Zhang, H., Lin, W., Wang, Y., Xu, W., and Jia, S.: First simultaneous measurements of peroxyacetyl  
762 nitrate (PAN) and ozone at Nam Co in the central Tibetan Plateau: impacts from the PBL evolution and transport  
763 processes, *Atmos. Chem. Phys.*, 18, 5199–5217, <https://doi.org/10.5194/acp-18-5199-2018>, 2018.

764 [74] Bi, H., Chen, S., Zhao, D., Lu, F., Chen, Y., and Guan, Y.: Aerosol optical properties and its direct radiative  
765 forcing over Tibetan Plateau from 2006 to 2017, *Particuology*, 74, 64–73, <https://doi.org/10.1016/j.partic.2022.05.007>,  
766 2023.

767 [75] Yang, J., Kang, S., and Ji, Z.: Critical contribution of south Asian residential emissions to atmospheric black  
768 carbon over the Tibetan plateau, *Sci. Total Environ.*, 709, 135923, <https://doi.org/10.1016/j.scitotenv.2019.135923>,  
769 2020.

770 [76] Zhang, X., Ming, J., Li, Z., Wang, F., and Zhang, G.: The online measured black carbon aerosol and source  
771 orientations in the Nam Co region, Tibet, *Environ. Sci. Pollut. Res.*, 24, 25021–25033, doi:  
772 10.1007/s11356-017-0165-1, 2017.

773 [77] Yang, J., Duan, K., Kang, S., Shi, P., and Ji, Z.: Potential feedback between aerosols and meteorological  
774 conditions in a heavy pollution event over the Tibetan Plateau and Indo-Gangetic Plain, *Clim. Dyn.*, 48(9), 2901–2917,  
775 doi:10.1007/s00382-016-3240-2, 2017.

776 [78] Wan, X., Kang, S., Wang, Y., Xin, J., Liu, B., Guo, Y., Wen, T., Zhang, G., and Cong, Z.: Size distribution of  
777 carbonaceous aerosols at a high-altitude site on the central Tibetan Plateau (Nam Co Station, 4730 m a.s.l.), *Atmos.*  
778 *Res.* 153, 155–164, doi:10.1016/j.atmosres.2014.08.008, 2015.

779 [79] Li, C., Bosch, C., Kang, S., Andersson, A., Chen, P., Zhang, Q., Cong, Z., Chen, B., Qin, D., and Gustafsson, O.:  
780 Sources of black carbon to the Himalayan-Tibetan Plateau glaciers, *Nat. Commun.*, 7, 12574,  
781 doi:10.1038/ncomms12574, 2016.

782 [80] Lei, Y., Yang, K., Wang, B., Sheng, Y., Bird, B.W., Zhang, G., and Tian, L.: Response of inland lake dynamics  
783 over the Tibetan Plateau to climate change, *Clim. Chang.* 125, 281–290, doi:10.1007/210584-014-1175-3, 2014.

784 [81] Zhu, G., Guo, H., Qin, D., Pan, H., Jia, W., and Ma, X.: Contribution of recycled moisture to precipitation in the  
785 monsoon marginal zone: Estimate based on stable isotope data, *J. Hydrol.*, 569, 423–435,  
786 doi:10.1016/j.jhydrol.2018.12.014, 2019.

787 [82] Boxe, C.: *Nitrate photochemistry and interrelated chemical phenomena in ice*[M]. California Institute of  
788 Technology, 2005.

789 [83] Xu, R., Tie, X., Li, G., Zhao, S., Cao, J., Feng, T., and Long, X.: Effect of biomass burning on black carbon (BC)  
790 in South Asia and Tibetan Plateau: The analysis of WRF-Chem modeling, *Sci. Total Environ.*, 645, 901–912,  
791 doi:10.1016/j.scitotenv.2018.07.165, 2018.

792 [84] Neupane, B., Kang, S., Chen, P., Zhang, Y., Ram, K., Rupakheti, D., Tripathi, L., Sharma, C.M., Cong, Z., Li,  
793 C., Hou, J., Xu, M., and Thapa, P.: Historical black carbon reconstruction from the lake sediments of the  
794 Himalayan-Tibetan Plateau, *Environ. Sci. Tech.*, 53, 5641–5651, doi:10.1021/acs.est.8b07025, 2019.

795 [85] Xu, K., Zhong, L., Ma, Y., Zou, M., and Huang, Z.: A study on the water vapor transport trend and water vapor  
796 sources of the Tibetan Plateau, *Theor. Appl. Climatol.*, 140, 1031–1042, doi:10.1007/s00704-020-03142-2, 2020.

797 [86] Xu, Y., Kang, S., Zhang, Y., and Zhang, Y.: A method for estimating the contribution of evaporative vapor from  
798 Nam Co to local atmospheric vapor based on stable isotopes of water bodies, *Chinese Sci. Bull.*, 56(14), 1511–1517,  
799 doi:10.1007/s11434-011-4467-2, 2011.

- 800 [87] Chen, P., Kang, S., Yang, J., Pu, T., Li, C., Guo, J., and Tripathee, L.: Spatial and temporal variations of gaseous  
801 and particle pollutants in six sites in Tibet, China, during 2016-2017, *Aerosol Air Qual. Res.*, 19, 516-527,  
802 doi:10.4209/aaqr.2018.10.0360, 2019.
- 803 [88] Wang, T., Xue, L., Brimblecombe, P., Lam, Y, Li, L. and Zhang, L.: Ozone pollution in China: A review of  
804 concentrations, meteorological influences, chemical precursors, and effects. *Sci. Total Environ.*, 575, 1582–1596,  
805 doi:10.1016/j.scitotenv.2016.10.081, 2017.
- 806 [89] Pokharel, M., Guang, J., Liu, B., Kang, S., Ma, Y., Holben, B.N., Xia, X., Xin, J., Ram, K., Rupakheti, D., Wan,  
807 X., Wu, G., Bhattarai, H., Zhao, C., and Cong, Z.: Aerosol properties over Tibetan Plateau from a decade of  
808 AERONET measurements: Baseline, types, and influencing factors, *J. Geophys. Res.: Atmos.*, 124, 13357-13374,  
809 doi:10.1029/2019JD031293, 2019.
- 810 [90] Cong, Z., Kang, S., Smirnov, A., and Holben, B.: Aerosol optical properties at Nam Co, a remote site in central  
811 Tibetan Plateau, *Atmos. Res.*, 92, 42-48, doi:10.1016/j.atmosres.2008.08.005, 2009.
- 812 [91] Qian, Y., Wang, H., Zhao, C., Zhao, C., Chen, S., Hu, X., and Kang, S.: Understanding third pole atmospheric  
813 dynamics and land surface processes and their associations with the cryosphere, air quality, and climate change, *Adv.*  
814 *Atmos. Sci.*, 39, 1017-1020, doi:10.1007/s00376-022-2004-7, 2022.
- 815 [92] Xu, L., Liu, H., Du, Q., and Xu, X.: The assessment of the planetary boundary layer schemes in WRF over the  
816 central Tibetan Plateau, *Atmos. Res.*, 230, 104644, doi:10.1016/j.atmosres.2019.104644, 2019.
- 817 [93] Yang, J., and Duan, K.: Effects of initial drivers and land use on WRF modeling for near-surface fields and  
818 atmospheric boundary layer over the northeastern Tibetan Plateau, *Adv. Meteorol.*, 2016, 7849249,  
819 doi:10.1155/2016/7849249, 2016.
- 820 [94] Kleffmann, J., Gavriloiu, T., Hofzumahaus, A., Holland, F., Koppmann, R., Rupp, L., Schlosser, E., Siese, M.,  
821 and Wahner, A.: Daytime formation of nitrous acid: A major source of OH radicals in a forest, *Geophys. Res. Lett.*,  
822 32(5), doi:10.1029/2005GL022524, 2005.
- 823 [95] Su, H., Cheng, Y., Shao, M., Gao, D., Yu, Z., Zeng, L., Slanina, J., Zhang, Y., and Wiedensohler, A.: Nitrous  
824 acid (HONO) and its daytime sources at a rural site during the 2004 PRIDE-PRD experiment in China, *J. Geophys.*  
825 *Res.*, 113, D14312, doi:10.1029/2007JD009060, 2008.
- 826 [96] Yang, Y., Li, X., Zu, K., Lian, C., Chen, S., Dong, H., Feng, M., Liu, H., Liu, J., Lu, K., Lu, S., Ma, X., Song, D.,  
827 Wang, W., Yang, S., Yang, X., Yu, X., Zhu, Y., Zeng, L., Tan, Q., and Zhang, Y.: Elucidating the effect of HONO  
828 and O<sub>3</sub> pollution by a case study in southwest China, *Sci. Total Environ.*, 756, 144127,  
829 doi:10.1016/j.scitotenv.2020.144127, 2021.
- 830 [97] Liu, T., Hong, Y., Li, M., Xu, L., Chen, J., Bian, Y., Yang, C., Dan, Y., Zhang, Y., Xue, L., Zhao, M., Huang, Z.,  
831 and Wang, H.: Atmospheric oxidation capacity and ozone pollution mechanism in a coastal city of southeastern China:  
832 analysis of a typical photochemical episode by an observation-based model, *Atmos. Chem. Phys.*, 22, 2173-2190,  
833 doi:10.5194/acp-22-2173-2022, 2022.
- 834 [98] Xu, S., Wang, S., Xia, M., Lin, H., Xing, C., Ji, X., Su, W., Tan, W., Liu, C., and Hu, Q.: Observations by  
835 ground-based MAX-DOAS of the vertical characters of winter pollution and the influencing factors of HONO  
836 generation in Shanghai, China, *Remote Sens.*, 13, 3518, doi:10.3390/rs13173518, 2021.
- 837 [99] Hendrick, F., Müller, J.F., Clémer, K., Wang, P., De Mazière, M., Fayt, C., Gielen, C., Hermans, C., Ma, J.,  
838 Pinardi, G., Stavrou, T., Vlemmix, T., Van Roozendaal, M.: Four years of ground-based MAX-DOAS observations  
839 of HONO and NO<sub>2</sub> in the Beijing area, *Atmos. Chem. Phys.*, 14, 765–781, doi:10.5194/acp-14-765-2014, 2014.
- 840 [100] Cui, L., Li, R., Fu, H., Li, Q., Zhang, L., George, C., and Chen, J.: Formation features of nitrous acid in the  
841 offshore area of the East China Sea, *Sci. Total Environ.*, 682, 138-150, doi: 10.1016/j.scitotenv.2019.05.004, 2019.
- 842 [101] Yang, J., Shen, H., Guo, M., Zhao, M., Jiang, Y., Chen, T., Liu, Y., Li, H., Zhu, Y., Meng, H., Wang, W., and  
843 Xue, L.: Strong marine-derived nitrous acid (HONO) production observed in the coastal atmosphere of northern  
844 China, *Atmos. Environ.*, 244, 117948, doi: 10.1016/j.atmosenv.2020.117948, 2021.
- 845 [102] Liu, Y., Nie, W., Xu, Z., Wang, T., Wang, R., Li, Y., Wang, L., Chi, X., and Ding, A.: Semi-quantitative  
846 understanding of source contribution to nitrous acid (HONO) based on 1 year of continuous observation at the  
847 SORPES station in eastern China, *Atmos. Chem. Phys.*, 19, 13289–13308, doi: 10.5194/acp-19-13289-2019, 2019.
- 848 [103] Jena, C., Ghude, S.D., Pfister, G.G., Chate, D.M., Kumar, R., Beig, G., Surendran, D.E., Fadnavis, S., and Lal,  
849 D.M.: Influence of springtime biomass burning in South Asia on regional ozone (O<sub>3</sub>): A model based case study,  
850 *Atmos. Environ.*, 100, 37-47, doi:10.1016/j.atmosenv.2014.10.027, 2015.
- 851 [104] Xing, L., Bei, N., Guo, J., Wang, Q., Liu, S., Han, Y., Pongpiachan, S., and Li, G.: Impacts of biomass burning  
852 in peninsular southeast Asia on PM<sub>2.5</sub> concentration and ozone formation in southeastern China during springtime-A  
853 case study, *J. Geophys. Res.: Atmos.*, 126(22), e2021JD034908, doi:10.1029/2021JD034908, 2021.
- 854 [105] Kumar, R., Naja, M., Pfister, G.G., Barth, M.C., Wiedinmyer, C., and Brasseur, G.P.: Simulations over South  
855 Asia using the Weather Research and Forecasting model with Chemistry (WRF-Chem): chemistry evaluation and  
856 initial results, *Geosci. Model Dev.*, 5, 619–648, doi:10.5194/gmd-5-619-2012, 2012.
- 857 [106] Sharma, A., Ojha, N., Pozzer, A., Mar, K.A., Beig, G., Lelieveld, J., and Gunthe, S.S.: WRF-Chem simulated  
858 surface ozone over south Asia during the pre-monsoon: effects of emission inventories and chemical mechanisms,  
859 *Atmos. Chem. Phys.*, 17, 14393–14413, doi: 10.5194/acp-17-14393-2017, 2017.

- 860 [107] Cristofanelli, P., Bracci, A., Sprenger, M., Marinoni, A., Bonafè, U., Calzolari, F., Duchi, R., Laj, P., Pichon, J.  
861 M., Roccato, F., Venzac, H., Vuillermoz, E., and Bonasoni, P.: Tropospheric ozone variations at the Nepal Climate  
862 Observatory Pyramid (Himalayas, 5079 m a.s.l.) and influence of deep stratospheric intrusion events, *Atmos. Chem.*  
863 *Phys.*, 10, 6537–6549, doi:10.5194/acp-10-6537-2010, 2010.
- 864 [108] Chen, X. L., Ma, Y. M., Kelder, H., Su, Z., and Yang, K.: On the behaviour of the tropopause folding events  
865 over the Tibetan Plateau, *Atmos. Chem. Phys.*, 11, 5113–5122, doi:10.5194/acp-11-5113-2011, 2011.
- 866 [109] Škerlak, B., Sprenger, M., and Wernli, H.: A global climatology of stratosphere–troposphere exchange using the  
867 ERA-Interim data set from 1979 to 2011, *Atmos. Chem. Phys.*, 14, 913–937, doi:10.5194/acp-14-913-2014, 2014.
- 868 [110] Putero, D., Cristofanelli, P., Sprenger, M., Škerlak, B., Tositti, L., and Bonasoni, P.: STEFLUX, a tool for  
869 investigating stratospheric intrusions: application to two WMO/GAW global stations, *Atmos. Chem. Phys.*, 16,  
870 14203–14217, doi:10.5194/acp-16-14203-2016, 2016.
- 871 [111] Fu, X., Wang, T., Zhang, L., Li, Q., Wang, Z., Xia, M., Yun, H., Wang, W., Yu, C., Yue, D., Zhou, Y., Zheng,  
872 J., and Han, R.: The significant contribution of HONO to secondary pollutants during a severe winter pollution event  
873 in southern China, *Atmos. Chem. Phys.*, 19, 1–14, doi: 10.5194/acp-19-1-2019, 2019.
- 874 [112] Ren, Y., Stieger, B., Spindler, G., Grosselin, B., Mellouki, A., Tuch, T., Wiedensohler, A., and Herrmann, H.:  
875 Role of the dew water on the ground surface in HONO distribution: a case measurement in Melpitz, *Atmos. Chem.*  
876 *Phys.*, 20, 13069–13089, doi: 10.5194/acp-20-13069-2020, 2020.
- 877 [113] Crilley, L.R., Kramer, L.J., Pope, F.D., Reed, C., Lee, J.D., Carpenter, L.J., Hollis, L.D.J., Ball, S.M., and Bloss,  
878 W.J.: Is the ocean surface a source of nitrous acid (HONO) in the marine boundary layer? *Atmos. Chem. Phys.*, 21,  
879 18213–18225, doi: 10.5194/acp-21-18213-2021, 2021.
- 880 [114] Li, S., Song, W., Zhan, H., Zhang, Y., Zhang, X., Li, W., Tong, S., Pei, C., Wang, Y., Chen, Y., Huang, Z.,  
881 Zhang, R., Zhu, M., Fang, H., Wu, Z., Wang, J., Luo, S., Fu, X., Xiao, S., Huang, X., Zeng, J., Zhang, H., Chen, D.,  
882 Gligorovski, S., Ge, M., George, C., and Wang, X.: Contribution of vehicle emission and NO<sub>2</sub> surface conversion to  
883 nitrous acid (HONO) in urban environments: Implications from tests in a tunnel, *Environ. Sci. Technol.*, 55(23),  
884 15616–15624, doi:10.1021/acs.est.1c00405, 2021.
- 885 [115] Chai, J., Dibb, J.E., Anderson, B.E., Bekker, C., Blum, D.E., Heim, E., Jordan, C.E., Joyce, E.E., Kaspari, J.H.,  
886 Munro, H., Walters, W.W., and Hastings, M.G.: Isotopic evidence for dominant secondary production of HONO in  
887 near-ground wildfire plumes, *Atmos. Chem. Phys.*, 21, 13077–13098, doi: 10.5194/acp-21-13077-2021, 2021.
- 888 [116] Cui, L., and Wang, S.: Mapping the daily nitrous acid (HONO) concentrations across China during 2006–2017  
889 through ensemble machine-learning algorithm, *Sci. Total Environ.*, 785, 147325, doi:10.1016/j.scitotenv.2021.147325,  
890 2021.
- 891 [117] Cui, L., Li, R., Fu, H., Meng, Y., Zhao, Y., Li, Q., and Chen, J.: Nitrous acid emission from open burning of  
892 major crop residues in mainland China, *Atmos. Environ.*, 244, 117950, doi:10.1016/j.atmosenv.2020.117950, 2021.
- 893 [118] Su, H., Cheng, Y., Oswald, R., Behrendt, T., Trebs, I., Meixner, F.X., Andreae, M.O., Cheng, P., Zhang, Y., and  
894 Poschl, U.: Soil nitrite as a source of atmospheric HONO and OH radicals, *Science*, 333(6049), 1616–1618,  
895 doi:10.1126/science.1207687, 2011.
- 896 [119] Lin, F., Liu, C., Hu, X., Fu, Y., Zheng, X., Wang, R., Zhang, W., and Cao, G.: Characterizing nitric oxide  
897 emissions from two typical alpine ecosystems, *J. Environ. Sci.*, 77, 312–322, doi:10.1016/j.jes.2018.08.011, 2019.
- 898 [120] Gil, J., Kim, J., Lee, M., Lee, G., Lee, D., Jung, J., An, J., Hong, J., Cho, S., Lee, J., and Long, R.: The role of  
899 HONO in O<sub>3</sub> formation and insight into its formation mechanism during the KORUS-AQ Campaign, *Atmos. Chem.*  
900 *Phys. Discuss.*, doi: 10.5194/acp-2019-1012, 2019.
- 901 [121] Wen, L., Chen, T., Zheng, P., Wu, L., Wang, X., Mellouki, A., Xue, L., and Wang, W.: Nitrous acid marine  
902 boundary layer over eastern Bohai Sea, China: Characteristics, sources, and implications, *Sci. Total Environ.*, 670,  
903 282–291, doi:10.1016/j.scitotenv.2019.03.225, 2019.
- 904 [122] Lu, X., Wang, Y., Li, J., Shen, L., and Fung, J.C.H.: Evidence of heterogeneous HONO formation from aerosols  
905 and the regional photochemical impact of this HONO source, *Environ. Res. Lett.* 13, 114002,  
906 doi:10.1088/1748-9326aae492, 2018.
- 907 [123] Cui, L., Li, R., Zhang, Y., Meng, Y., Fu, H., and Chen, J.: An observational study of nitrous acid (HONO) in  
908 Shanghai, China: The aerosol impact on HONO formation during the haze episodes, *Sci. Total Environ.*, 630,  
909 1057–1070, doi:10.1016/j.scitotenv.2018.02.063, 2018.
- 910 [124] Wang, S., Zhou, R., Zhao, H., Wang, Z., Chen, L., and Zhou, B.: Long-term observation of atmospheric nitrous  
911 acid (HONO) and its implication to local NO<sub>2</sub> levels in Shanghai, China, *Atmos. Environ.*, 77, 718–724,  
912 doi:10.1016/j.atmosenv.2013.05.071, 2013.
- 913 [125] Meng, F., Qin, M., Tang, K., Duan, J., Fang, W., Liang, S., Ye, K., Xie, P., Sun, Y., Xie, C., Ye, C., Fu, P., Liu,  
914 J., and Liu, W.: High-resolution vertical distribution and sources of HONO and NO<sub>2</sub> in the nocturnal boundary layer  
915 in urban Beijing, China, *Atmos. Chem. Phys.*, 20, 5071–5092, doi: 10.5194/acp-20-5071-2020, 2020.
- 916 [126] Zhang, W., Tong, S., Jia, C., Wang, L., Liu, B., Tang, G., Ji, D., Hu, B., Liu, Z., Li, W., Wang, Z., Liu, Y.,  
917 Wang, Y., and Ge, M.: Different HONO sources for three layer at the urban area of Beijing, *Environ. Sci. Technol.*,  
918 54, 12870–12880, doi:10.1021/acs.est.0c02146, 2020.

- 919 [127] Fang, X., Li, T., Ban, C., Wu, Z., Li, J., Li, F., Cen, Y., and Tian, B.: A mobile differential absorption lidar for  
920 simultaneous observations of tropospheric and stratospheric ozone over Tibet, *Opt. Express*, 27(4), 4126-4139,  
921 doi:10.1364/OE.27.004126, 2019.
- 922 [128] Yu, J., Meng, L., Chen, Y., Zhang, H., and Liu, J.: Ozone profiles, precursors, and vertical distribution in urban  
923 Lhasa, Tibetan Plateau, *Remote Sens.*, 14(11), doi:10.3390/rs14112533, 2022.
- 924 [129] Zhang, J., Xia, X., and Wu, X.: First in situ UV profile across the UTLS accompanied by ozone measurement  
925 over the Tibetan Plateau, *J. Environ. Sci.*, 98, 71-76, doi:10.1016/j.jes.2020.05.020.
- 926 [130] Fisher, F. N.: Extinction of UV-visible radiation in wet midlatitude (maritime) snow: Implications for increased  
927 NO<sub>x</sub> emission, *J. Geophys. Res.*, 110, D21301, doi:10.1029/2005JD005963, 2005.
- 928 [131] Lin, W., Wang, F., Ye, C., Zhu, T.: Observation of strong NO<sub>x</sub> release over Qiyi Glacier, China. *The*  
929 *Cryosphere*, doi.org/10.5194/tc-2021-32, 2021.
- 930 [132] Ji, X., Liu, C., Wang, Y., Hu, Q., Lin, H., Zhao, F., Xing, C., Tang, G., Zhang, J., Wagner, T.: Ozone profiles  
931 without blind area retrieved from MAX-DOAS measurements and comprehensive validation with multi-platform  
932 observations. *Remote Sens. Environ.*, 284, 113339, doi.org/10.1016/j.res.2022.113339, 2023.
- 933 [133] Lin, H., Liu, C., Xing, C., Hu, Q., Hong, Q., Liu, H., Li, Q., Tan, W., Ji, X., Wang, Z., Liu, J.: Validation of  
934 water vapor vertical distributions retrieved from MAX-DOAS over Beijing, China. *Remote Sens.*, 12, 3193,  
935 doi.org/10.3390/rs12193193, 2020.
- 936 [134] Xing, C., Xu, S., Song, Y., Liu, C., Liu, Y., Lu, K., Tan, W., Zhang, C., Hu, Q., Wang, S., Wu, H., Lin, H.: A  
937 new insight into the vertical differences in NO<sub>2</sub> heterogeneous reaction to produce HONO over inland and marginal  
938 seas. *Atmos. Chem. Phys.*, 23, 5815-5834, doi.org/10.5194/acp-23-5815-2023, 2023.
- 939 [135] Rodgers, C. D.: Inverse methods for atmospheric sounding: theory and practice. Singapore-New  
940 Jersey-London-Hong: World Scientific Publishing; 2000.
- 941 [136] Wagner, T., Dix, B., FriedeBurg, C. V., Frieß, U., Sanghavi, S., Sinreich, R., Platt, U.: MAX-DOAS O<sub>4</sub>  
942 measurements: A new technique to derive information on atmospheric aerosols-Principles and information content. *J.*  
943 *Geophys. Res.: Atmos.*, 109, D22205, doi.org/10.1029/2004jd004904, 2004.
- 944 [137] Serdyuchenko, A., Gorshelev, V., Weber, M., Chehade, W., Burrows, J. P.: High spectral resolution ozone  
945 absorption cross-sections-Part 2: Temperature dependence. *Atmos. Meas. Tech.*, 7, 625-636,  
946 doi:10.5194/amt-7-625-2014, 2014.
- 947 [138] Wang, Y., Lampel, J., Xie, P., Beirle, S., Li, A., Wu, D., Wagner, T.: Ground-based MAX-DOAS observations  
948 of tropospheric aerosols, NO<sub>2</sub>, SO<sub>2</sub> and HCHO in Wuxi, China, from 2011 to 2014. *Atmos. Chem. Phys.*, 17,  
949 2189-2215, doi.org/10.5194/acp-17-2189-2017, 2017.
- 950 [139] Wang, Y., Apituley, A., Bais, A., Beirle, S., Benavent, N., Borovski, A., Bruchkouski, I., Chan, K. L., Donner,  
951 S., Drosoglou, T., Finkenzeller, H., Friedrich, M. M., Frieß, U., Garcia-Nieto, D., Gómez-Martín, L., Hendrick, F.,  
952 Hilboll, A., Jin, J., Johnston, P., Koenig, T. K., Kreher, K., Kumar, V., Kyuberis, A., Lampel, J., Liu, C., Liu, H., Ma,  
953 J., Polyansky, O. L., Postlyakov, O., Querel, R., Saiz-Lopez, A., Schmitt, S., Tian, X., Tirpitz, J. L., Van Roozendaal,  
954 M., Volkamer, R., Wang, Z., Xie, P., Xing, C., Xu, J., Yela, M., Zhang, C., Wagner, T.: Inter-comparison of  
955 MAX-DOAS measurements of tropospheric HONO slant column densities and vertical profiles during the CINDI-2  
956 campaign. *Atmos. Meas. Tech.*, 13, 5087–5116, doi.org/10.5194/amt-13-5087-2020, 2020.
- 957 [140] Thalman, R., Volkamer, R.: Temperature dependent absorption cross-sections of O<sub>2</sub>-O<sub>2</sub> collision pairs between  
958 340 and 630 nm and at atmospherically relevant pressure. *Phys. Chem. Chem. Phys.*, 15, 15371-15381,  
959 doi:10.1039/C3CP50968K, 2013.
- 960 [141] Vandaele, A. C., Hermans, C., Simon, P. C., Carleer, M., Colin, R., Fally, S., Merienne, M. F., Jenouvrier, A.,  
961 Coquart, D.: Measurements of the NO<sub>2</sub> absorption cross-section from 42000 cm<sup>-1</sup> to 10000 cm<sup>-1</sup> (238–1000nm) at  
962 220K and 294K. *J. Quant. Spectrosc. Ra.*, 59, 171-184, doi:10.1016/S0022-4073(97)00168-4, 1998.
- 963 [142] Stutz, J., Kim, E. S., Platt, U., Bruno, P., Perrino, C., Febo, A.: UV-visible absorption cross sections of nitrous  
964 acid. *J. Geophys. Res.: Atmos.*, 105, 14585-14592, doi:10.1029/2000JD900003, 2000.
- 965 [143] Aliwell, S. R., Van Roozendaal, M., Johnston, P. V., Richter, A., Wagner, T., Arlander, D. W., Burrows, J. P.,  
966 Fish, D. J., Jones, R. L., Tørnkqvist, K. K., Lambert, J. C., Pfeilsticker, K., and Pundt, I.: Analysis for BrO in  
967 zenith-sky spectra: an intercomparison exercise for analysis improvement, *J. Geophys. Res.*, 107, ACH 10-1–ACH  
968 10-20, <https://doi.org/10.1029/2001JD000329>, 2002.
- 969 [144] Vandaele, A. C., Hermans, C., Simon, P. C., Carleer, M., Colin, R., Fally, S., Mérienne, M. F., Jenouvrier, A.,  
970 and Coquart, B.: Measurements of the NO<sub>2</sub> absorption cross section from 42000 cm<sup>-1</sup> to 10000 cm<sup>-1</sup> (238–1000nm) at  
971 220 K and 294 K, *J. Quant. Spectrosc. Ra.*, 59, 171–184, doi:10.1016/S0022-4073(97)00168, 1998.
- 972 [145] Meller, R. and Moortgat, G. K.: Temperature dependence of the absorption cross sections of formaldehyde  
973 between 223 and 323 K in the wavelength range 225–375nm, *J. Geophys. Res.*, 105, 7089–7101,  
974 doi:10.1029/1999JD901074, 2000.
- 975 [146] Volkamer, R., Spietz, P., Burrows, J., Platt, U.: High-resolution absorption cross-section of glyoxal in the  
976 UV-vis and IR spectral ranges, *J. Photochem. Photobiol. A Chem.*, 172, 35–46,  
977 doi:10.1016/j.jphotochem.2004.11.011, 2005.
- 978 [147] Rothman, L. S., Gordon, I. E., Barbe, A., Benner, D. C., Bernath, P. E., Birk, M., Boudon, V., Brown, L. R.,  
979 Campargue, A., Champion, J. P., Chance, K., Coudert, L. H., Dana, V., Devi, V. M., Fally, S., Flaud, J. M., Gamache,

980 R. R., Goldman, A., Jacquemart, D., Kleiner, I., Lacombe, N., Lafferty, W. J., Mandin, J. Y., Massie, S. T.,  
981 Mikhailenko, S. N., Miller, C. E., Moazzen-Ahmadi, N., Naumenko, O. V., Nikitin, A. V., Orphal, J., Perevalov, V. I.,  
982 Perrin, A., Predoi-Cross, A., Rinsland, C. P., Rotger, M., Simeckova, M., Smith, M. A. H., Sung, K., Tashkun, S. A.,  
983 Tennyson, J., Toth, R. A., Vandaele, A. C., Vander Auwera, J.: The HITRAN 2008 molecular spectroscopic database,  
984 *J. Quant. Spectrosc. Radiat. Transf.*, 110, 533–572, 2009.  
985 [148] Fleischmann, O. C., Hartmann, M., Burrows, J. P., and Orphal, J.: New ultraviolet absorption cross-sections of  
986 BrO at atmospheric temperatures measured by time-windowing Fourier transform spectroscopy, *J. Photoch. Photobio.*  
987 *A*, 168, 117–132, 2004.  
988 [149] Ward Jr, J. H.: Hierarchical grouping to optimize an objective function, *J. Am. Stat. Assoc.*, 58, 236-244, 1963.  
989 [150] Wang, Y., Zhang, X., Arimoto, R.: The contribution from distant dust sources to the atmospheric particulate  
990 matter loading at XiAn, China during spring, *Sci. Total Environ.*, 368, 875-883, 2006.  
991 [151] Cheng, S., Pu, G., Ma, J., Hong, H., Du, J., Yudron, T., Wagner, T.: Retrieval of tropospheric NO<sub>2</sub> vertical  
992 column densities from ground-based MAX-DOAS measurements in Lhasa, a city on the Tibetan Plateau, *Remote*  
993 *Sens.*, 15, 4689, 2023a.  
994 [152] Cheng, S., Ma, J., Zheng, A., Gu, M., Donner, S., Donner, S., Zhang, W., Du, J., Li, X., Liang, Z., Lv, J.,  
995 Wagner, T.: Retrieval of O<sub>3</sub>, NO<sub>2</sub>, BrO and OCIO columns from ground-based zenith scattered light DOAS  
996 measurements in summer and autumn over the Northern Tibetan Plateau, *Remote Sens.*, 13, 4242, 2021.  
997 [153] Ma, J., Donner, S., Donner, S., Jin, J., Cheng, S., Guo, J., Zhang, Z., Wang, J., Liu, P., Zhang, G., Pukite, J.,  
998 Lampel, J., Wagner, T.: MAX-DOAS measurements of NO<sub>2</sub>, SO<sub>2</sub>, HCHO, and BrO at the Mt. Waliguan WMO GAW  
999 global baseline station in the Tibetan Plateau, *Atmos. Chem. Phys.*, 20, 6973-6990, 2020.  
1000 [154] Cheng, S., Cheng, X., Ma, J., Xu, X., Zhang, W., Lv, J., Bai, G., Chen, B., Ma, S., Ziegler, S., Donner, S.,  
1001 Wagner, T.: Mobile MAX-DOAS observations of tropospheric NO<sub>2</sub> and HCHO during summer over the Three  
1002 Rivers' Source region in China, *Atmos. Chem. Phys.*, 23, 3655-3677, 2023b.  
1003 [155] Li, M., Mao, J., Chen, S., Bian, J., Bai, Z., Wang, X., Chen, W., Yu, P.: Significant contribution of lightning  
1004 NO<sub>x</sub> to summertime surface O<sub>3</sub> on the Tibetan Plateau, *Sci. Total Environ.*, 829, 154639, 2022.  
1005  
1006